ON BAND FORMATION IN A NEW ENGLAND WINTER STORM

by

DAWN GUSTINE WOLFSBERG

B.S., University of California, Los Angeles

(1982)

SUBMITTED TO THE DEPARTMENT OF

EARTH, ATMOSPHERIC AND PLANETARY SCIENCES

IN PARTIAL FULFILLMENT OF THE

REQUIREMENTS FOR THE DEGREE OF

MASTER OF SCIENCE

at the

MASSACHUSETTS INSTITUTE OF TECHNOLOGY

May 1984

Signature of Auth
I ...d Planetary Scienc

Certif:

T'

Accepted by

Chairman, Departmental Co

ON BAND FORMATION IN A NEW ENGLAND WINTER STORM

by
DAWN GUSTINE WOLFSBERG

Submitted to the Department of
Earth, Atmospheric and Planetary Sciences
in partial fulfillment of the requirements for
the degree of Master of Science in
Meteorology

ABSTRACT

This case study addresses mechanisms of band formation in a New England winter storm. The structure of the bands and their environment are documented with synoptic observations, Doppler radar data, and analyses of instrumented aircraft flights through the bands. The paper postulates that processes on three scales are responsible for the bands observed. The bands are a manifestation of mesoscale symmetric instability. Potential energy for the instability is generated by synoptic scale differential lapse rate advection and converted to kinetic energy by the symmetric overturnings. There is a rough equilibrium between large scale generation and mesoscale depletion of potential energy. Frontogenetical forcing results in an intermediate or sub-synoptic scale region of ascent. The sub-synoptic scale vertical motion brings the atmosphere to saturation and enhances the release of potential energy.

Thesis Supervisor: Kerry A. Emanuel
Title: Assistant Professor of Meteorology

Index

page

Abstract.....2

Index.....3

Chapter I Introduction.....4

Chapter II Data and Experimental Design.....7

Chapter III Description of Bands.....10

Chapter IV Role of Symmetric Instability.....43

Chapter V Role of Frontogenetical Forcing.....71

Chapter VI Discussion and Conclusions.....94

Acknowledgements.....97

References.....98

I. INTRODUCTION

The purpose of this paper is to account for the formation of snow bands in a New England winter storm that was observed as part of a field project conducted by the Massachusetts Institute of Technology (MIT). On 11 December 1982, all of the precipitation in Central New England fell from weak, well-organized bands. It is argued that the bands are a manifestation of symmetric instability. The supply of potential energy available to the unstable motions represents an equilibrium between potential energy generation by large scale processes and conversion to kinetic energy by mesoscale processes. An intermediate or sub-synoptic scale region of ascent enhances release of the potential instability.

The two-dimensional cells frequently found in extra-tropical cyclones have attracted a great deal of attention. Linear organization of precipitation structures was noted by Austin (1960) in one of the first studies with weather radar. Houze et al. (1976) presented a comprehensive analysis of bands observed in cyclonic storms in the Pacific Northwest. They noted that bands can occur in every sector

of the storm. Elliot and Hovind (1964) observed a large number of bands in California and noted that the axes of the bands tend to lie along the mean vertical shear vector.

A number of mechanisms for band formation have been suggested. Harrold (1973) suggested that frontal circulations carry buoyant air to regions of band growth. Other possibilities include ducted gravity waves (Lindzen and Tung, 1976), density currents (Carbone, 1982), and symmetric instability (Emmanuel, 1979; Bennetts and Hoskins, 1978).

Some of these mechanisms can be ruled out in the present case. Harrold's "conveyor belt" model is not a candidate because there was very little thermal buoyancy. Although the temperature structure of the atmosphere may have allowed ducted gravity waves during the storm, evidence in the form of strong small scale pressure fluctuations was not found in microbarograph traces or in hourly pressure reports.

This paper is divided into six chapters. The experiment and data are described in chapter II. Chapter III is a description of the bands, which includes a discussion of important features in the large scale flow and analysis of band structure. Chapter IV discusses the role of symmetric instability. The theory and its predictions are reviewed. An expression for the time rate of change of potential energy for symmetric instability is derived. The susceptibility of the atmosphere to symmetric instability in this particular

case and the strength of updrafts which it would produce are evaluated. Estimates of potential energy depletion and generation rates are also given. Chapter V discusses the frontogenetical forcing. The strength of the forced updrafts and their effect on symmetric instability is considered. Chapter VI provides discussion and conclusions.

II. DATA AND EXPERIMENTAL DESIGN

Field observations for the case study include Doppler radar data, instrumented aircraft measurements, upper air data and surface observations. These are described below.

There are continuous observations from MIT's 11.03 cm wavelength Doppler radar for the 24 hour period of the case study, from 18 Greenwich Meridian Time (GMT) 10 December 1982, to 19 GMT 11 December 1982. Constant Altitude Plan Position Indicator (CAPPI) displays are analyzed for behavior of the bands. In additon, Waldteufel and Corbin's (1979) Volume Velocity Processing (VVP) technique is used to construct time-height cross sections of quantities derived from Doppler velocities.

At 1230 GMT and 1830 GMT, the Queenair, an instumented airplane from the National Center for Atmospheric Research, flew horizontal passes perpendicular to snow bands. The airplane instruments recorded temperature, velocity, humidity and cloud physical parameters every second. At both times there were four passes at approximately 1 km, 2 km, 3 km, and 4 km above the surface. Each pass was approximately 50 km long and was centered on the bands observed by the MIT radar. During the last half of the 1830 GMT flight the band moved in the band-normal direction. Bandpass cross sections derived from the airplane data are presented in band-relative

rather than physical coordinates. The coordinate axes were advected with the band. The band-relative cross band wind component was calculated by subtracting the x-component of the band-normal velocity of the band, 4 ms^{-1}, from the observed cross band velocity at each point in the 3 km and 4 km passes. The lower two bandpasses were completed while the band was stationary. In both flights, measurements varying by more than two standard deviations from a running mean were discarded. The data are averaged over ten seconds, or about one kilometer air distance, before analysis.

The National Meteorological Center's standard upper air and surface data are supplemented by special radiosonde launches at 12 GMT and 18 GMT at MIT. There are also special soundings at 18 GMT at Chatham, MA (CHH) and Albany, NY (ALB).

Fig. 1 shows the sites mentioned in this paper. The upper air network in the Northeast, and locations of the band passes and vertical cross section are indicated.

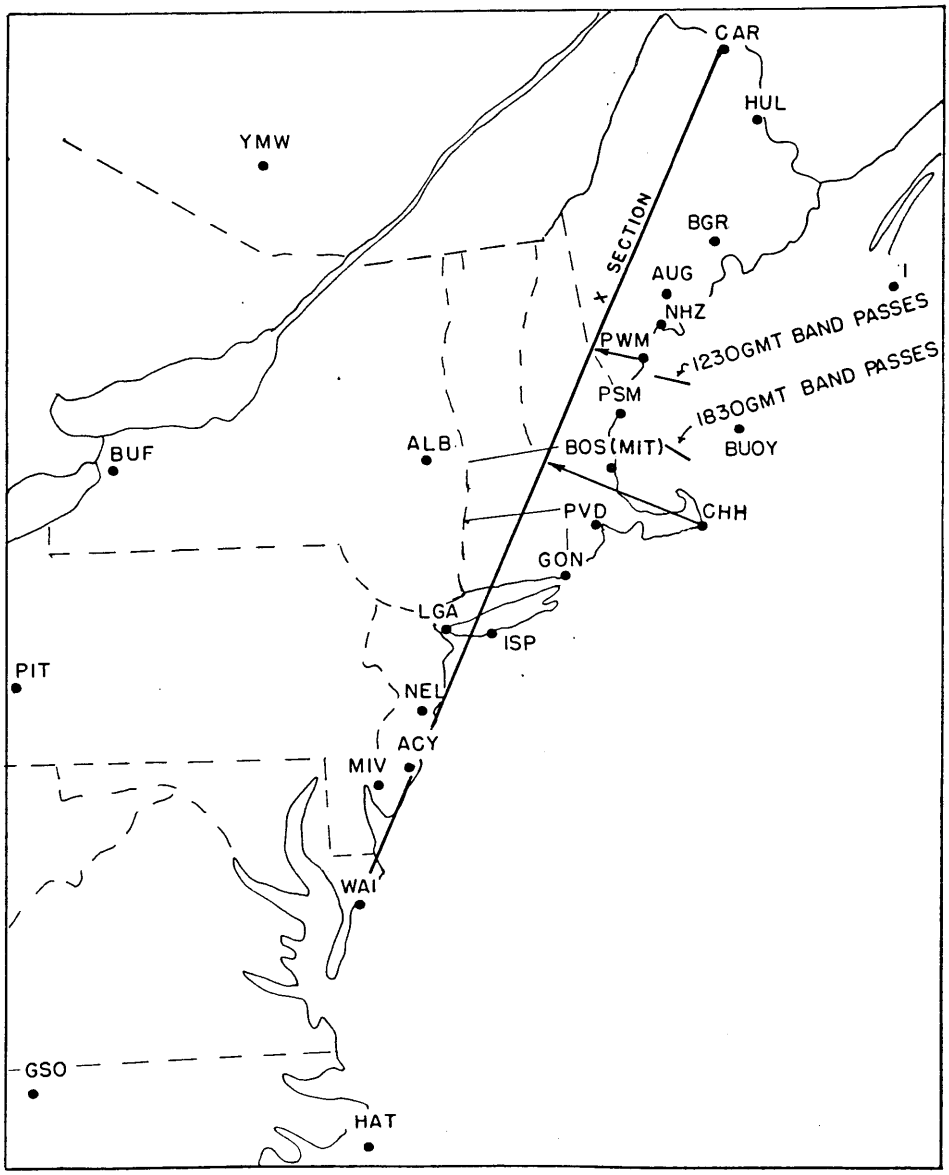

Fig. 1 Locations mentioned in the text. Stations mentioned or used in calculations are shown by three letter codes. A vertical cross section is shown by a dashed line. The locations of the band passes are indicated.

III. DESCRIPTION OF BANDS

The first radar echoes of the storm were observed on the MIT radar at 1930 GMT on 10 December. By 2230 GMT the echoes were organized into two bands. For the next 24 hours, bands continued to form and decay with lifespans of four to six hours each. The bands were well organized but very weak. Snowfall rates in New England never exceeded 2 $mmhr^{-1}$. In this section a detailed description of the bands is presented. The nature of the bands is explored through a discussion of the environment in which they formed, radar analysis and airplane bandpass analysis.

a. The Large Scale Environment

The synoptic scale weather pattern in New England is dominated by a deep cyclone centered on Hudson Bay. Figs. 2a-f show geopotential heights, winds, and temperatures at 850 mb, 700 mb,and 500 mb at 00 GMT and 12 GMT. The upper air flow over New England is in general west-southwesterly. The average large scale vertical shear is directed towards about 70° and exceeds 10^{-2} s^{-1} over deep layers. The geostrophic shear backs with height in some layers over New England, as can be seen in Fig. 2. The isobars are more southerly at 500mb than at at 850 mb at both 00 GMT and 12 GMT. This phenomenon is discussed in chapter IV.

Fig. 2 Upper air charts on 11 December 1982. Geopotential heights (solid lines) are drawn every 3 dam or 6 dam and isotherms (dashed lines) are drawn every 5°C. Winds are indicated with barbed velocity vectors. (1/2 barb = 5 kts, 1 barb = 10 kts, triangular barb = 50 kts. 1kt ≈ .5 ms^{-1})

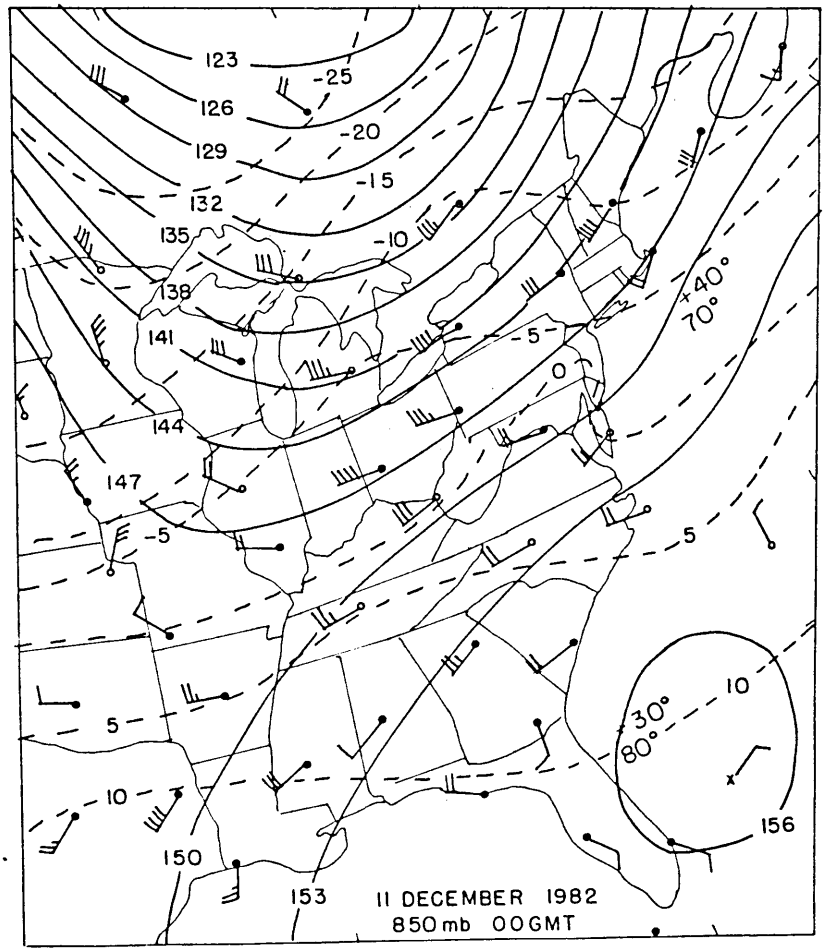
123
126
129
132
135
138
141
144
147
150
153
156
-25
-20
-15
-10
-5
0
5
10
+40°
70°
+30°
80°
11 DECEMBER 1982
850mb 00GMT

Fig. 2a

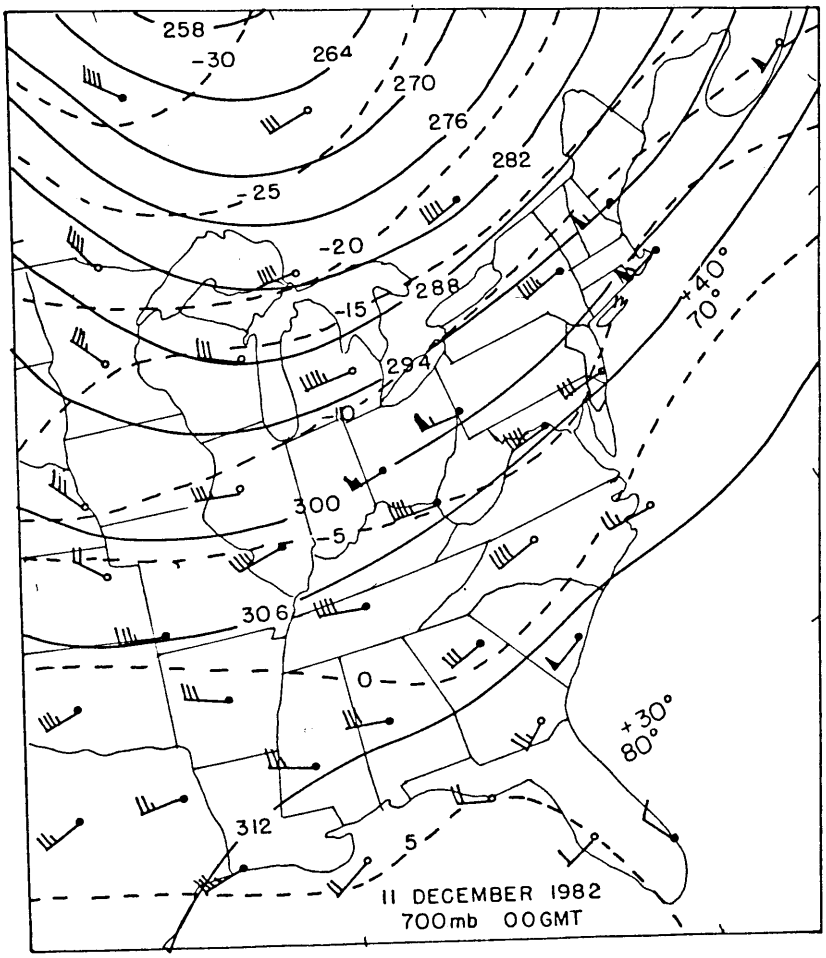
258
-30
264
270
276
282
-25
-20
288
-15
294
-10
300
-5
306
0
312
5
+40°
70°
+30°
80°
11 DECEMBER 1982
700mb 00GMT

Fig. 2b

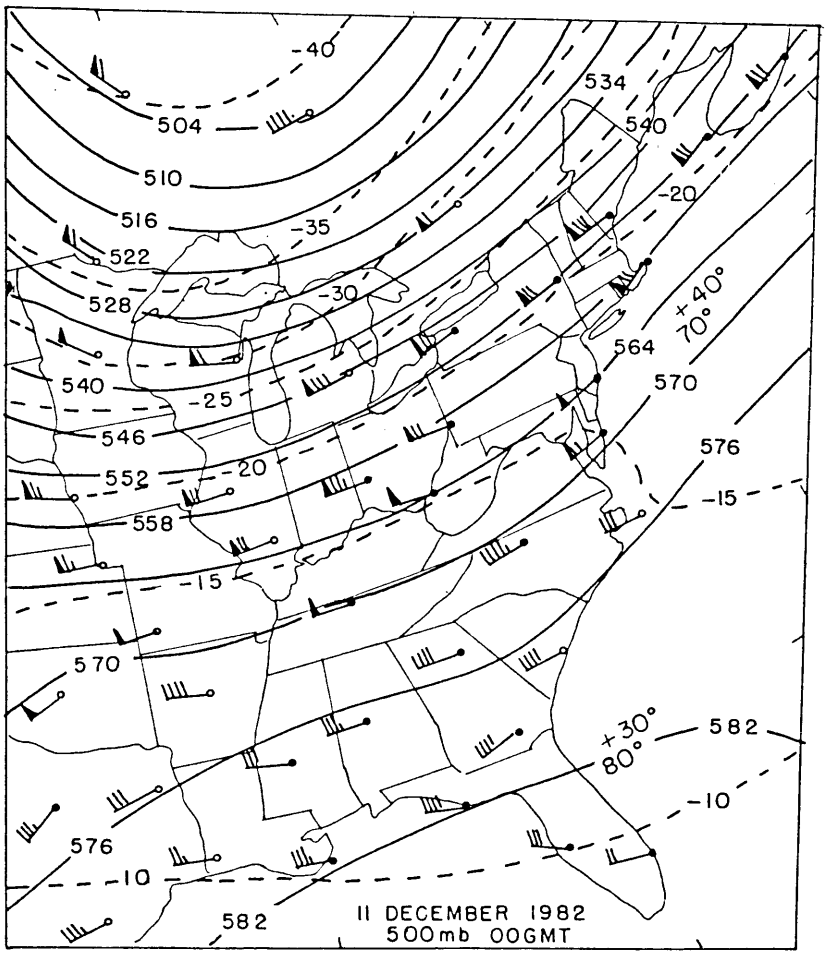
-40
504
510
516
522
528
540
546
552
558
570
576
582
534
540
564
570
576
582
-35
-30
-25
-20
-15
-10
+40°
70°
+30°
80°
11 DECEMBER 1982
500mb 00GMT

Fig. 2c

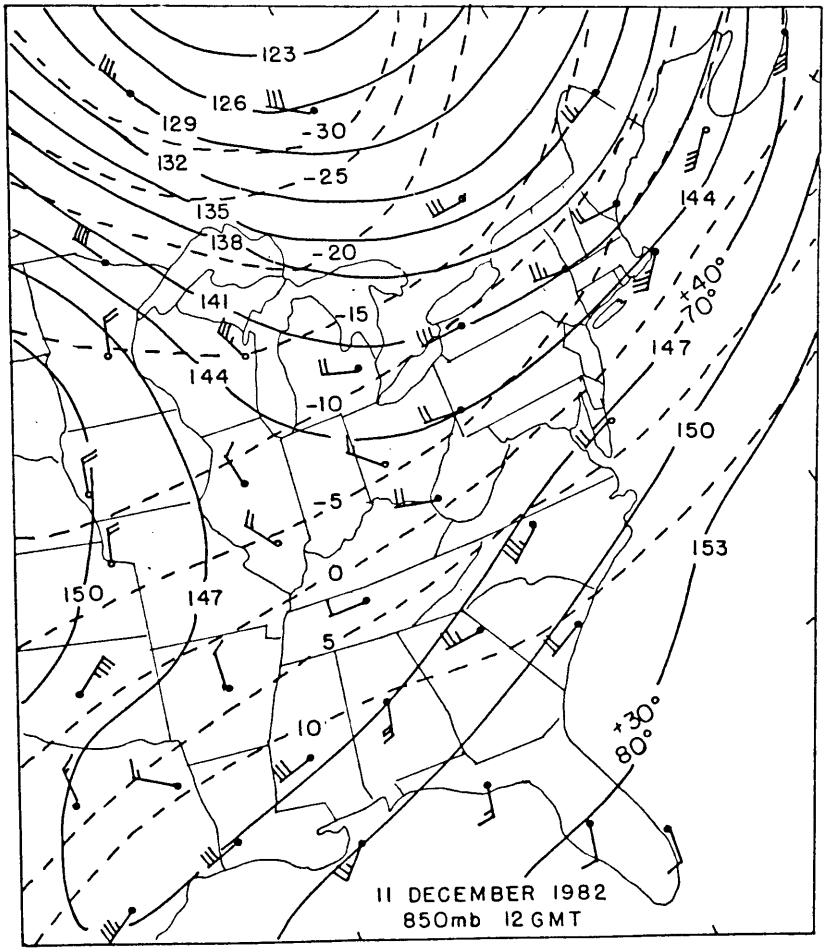
123
126
129
132
135
138
141
144
147
150
153
-30
-25
-20
-15
-10
-5
0
5
10
+40°
70°
+30°
80°
11 DECEMBER 1982
850mb 12 GMT

Fig. 2d

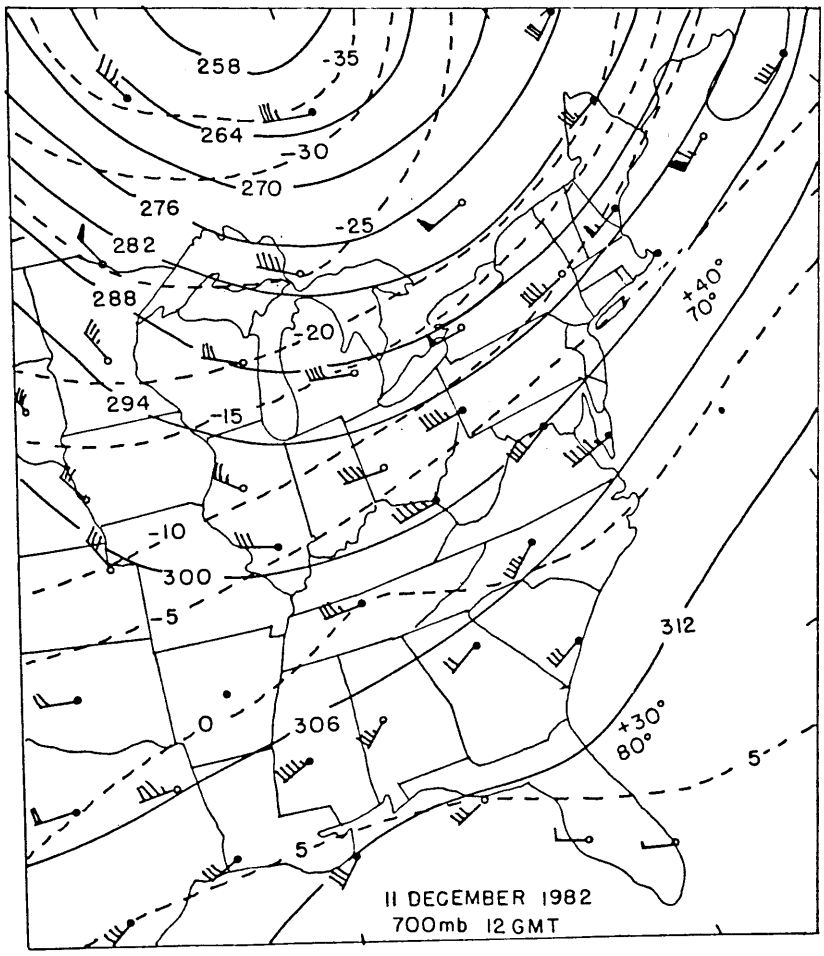
258
-35
264
-30
270
276
-25
282
288
-20
294
-15
-10
300
-5
312
0
306
+40°
70°
+30°
80°
5
5
11 DECEMBER 1982
700mb 12 GMT

Fig. 2e

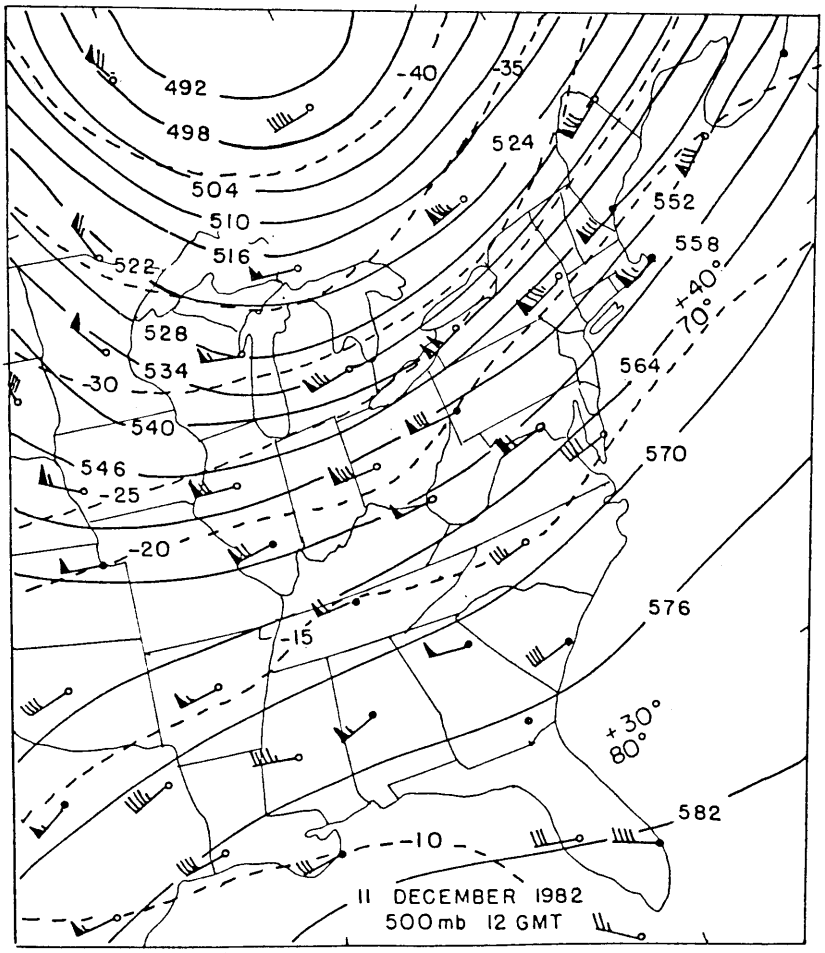
492
498
504
510
516
522
528
534
540
546
-40
-35
-30
-25
-20
-15
-10
524
552
558
564
570
576
582
+40°
70°
+30°
80°
11 DECEMBER 1982
500mb 12 GMT

Fig. 2f

The center of the storm and presumably the bulk of the upward motion are in the Great Plains area and in Tennessee, Alabama, and Georgia, well to the south and west of New England. As can be seen in Fig. 2, there is geostrophic warm advection at 850 mb at 00 GMT. However it is negligible at 700 mb at 00 GMT and at all levels at 12 GMT. The large scale upward motion can be estimated from a rough model of baroclinic instability. The synoptic scale vertical velocity is approximately half the horizontal wind speed times the slope of the potential temperature surfaces. This calculation yields large scale vertical velocities of less than 1 cms^{-1} at all levels over New England.

At 00 GMT the wind over New England at 850 mb and 700 mb is somewhat subgeostrophic. The velocities are generally in the direction of the isobars but with magnitudes typically 20% less than geostrophic values. The ageostrophy over New England becomes more pronounced at 12 GMT. At 850 mb (Fig. 2d), there is substantial ageostrophic warm advection at CHH and ageostrophic cold advection at PWM and ALB. There is also ageostrophic warm advection at CHH and ageostrophic cold advection at PWM at 700 mb. The deviation from geostrophy has a local maximum in New England. Its implications are discussed at greater length in chapters IV and V.

Figs. 3a-b show surface maps for 00 GMT and 12 GMT. The cold front west of Wisconsin at 00 GMT advances eastward at

about 8 ms^{-1} (30 $kmhr^{-1}$). It is ascertained with vertical cross sections oriented east to west (not shown) that there is very little east-west slope of potential isotherms over New England before about 18 GMT. The cold front probably does not affect the bands in New England until quite late in the case period. Note the warm fronts just south of Massachusetts and across the Southeast in Fig. 3. Forcing of the Massachusetts warm front is discussed in chapter V.

There is virtually no thermal buoyancy evident on soundings from stations in the Northeast. Most soundings show high stability in the boundary layer that sometimes extends into the lower troposphere. Soundings taken through the warm fronts show strong inversions. The air above the inversion is generally less stable. At many stations, the lapse rate through the middle to upper troposphere is almost moist adiabatic. These features are illustrated in Fig. 3c, which shows a typical sounding, the 00 GMT sounding for ALB on 11 December 1982. There is a thin unstable layer above the surface. There is high stability between 950 mb and 700 mb. The air is generally saturated below 600 mb. The strongest shear occurs between 650 mb and 700mb and is $2x10^{-2}$ s^{-1}. The atmosphere's thermal structure and other soundings are discussed at greater length in chapters IV and V.

Fig. 3a-b Surface charts on 11 December 1982. Isobars are drawn every 4 mb. The thousands and hundreds places are omited. Wind, temperature in °F, and present weather are indicated for each station.

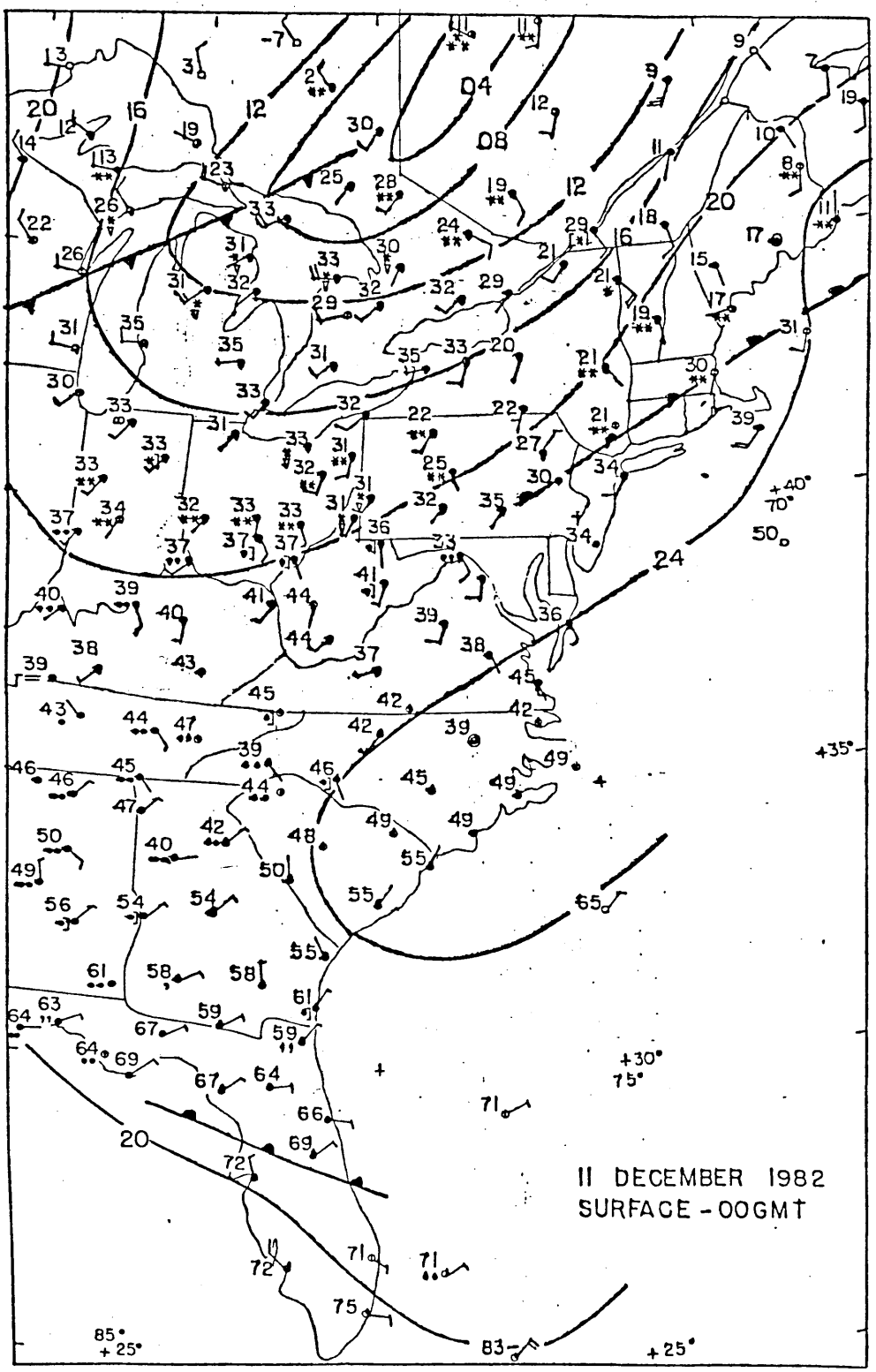

Fig. 3a

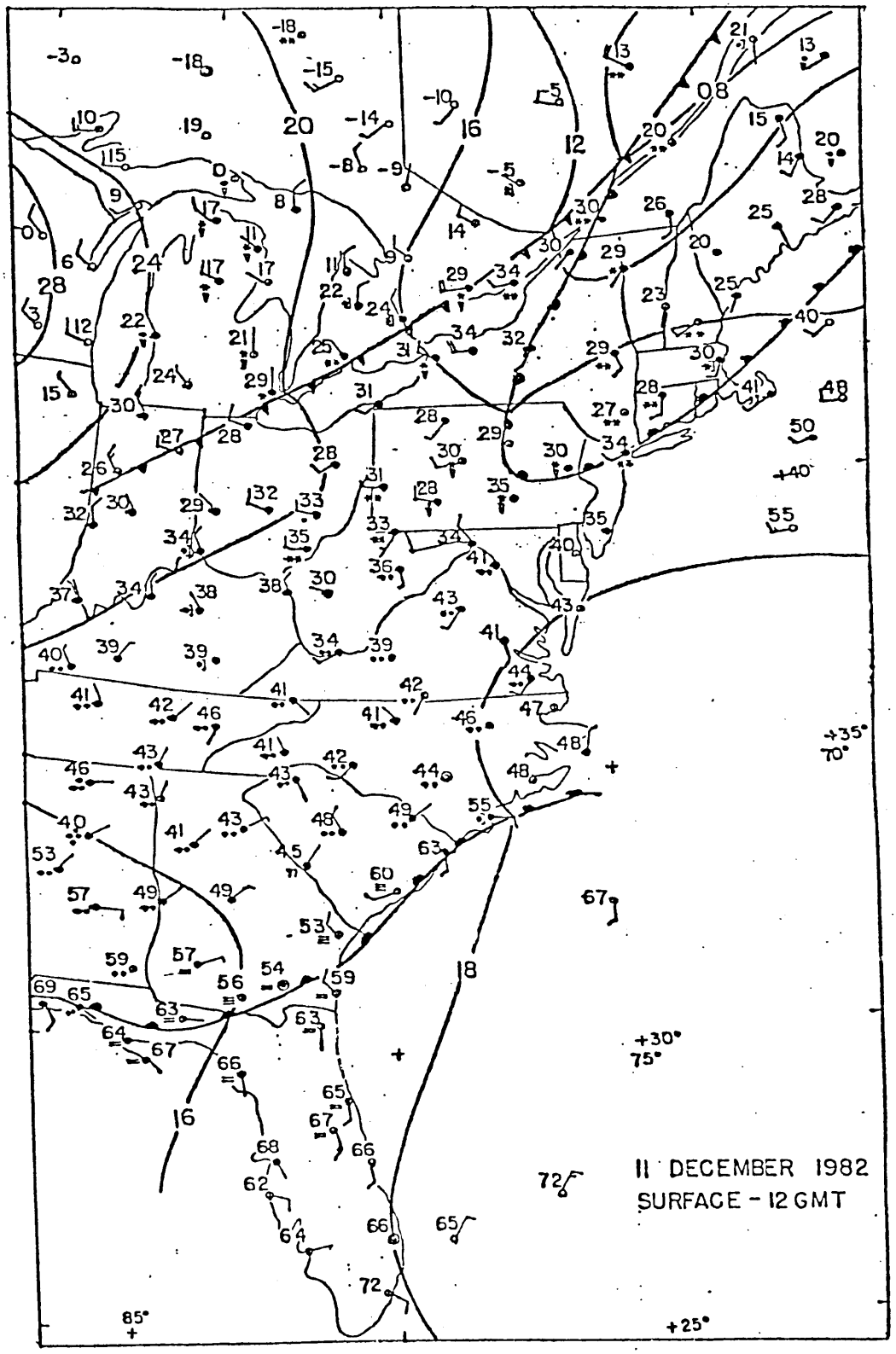

Fig. 3b

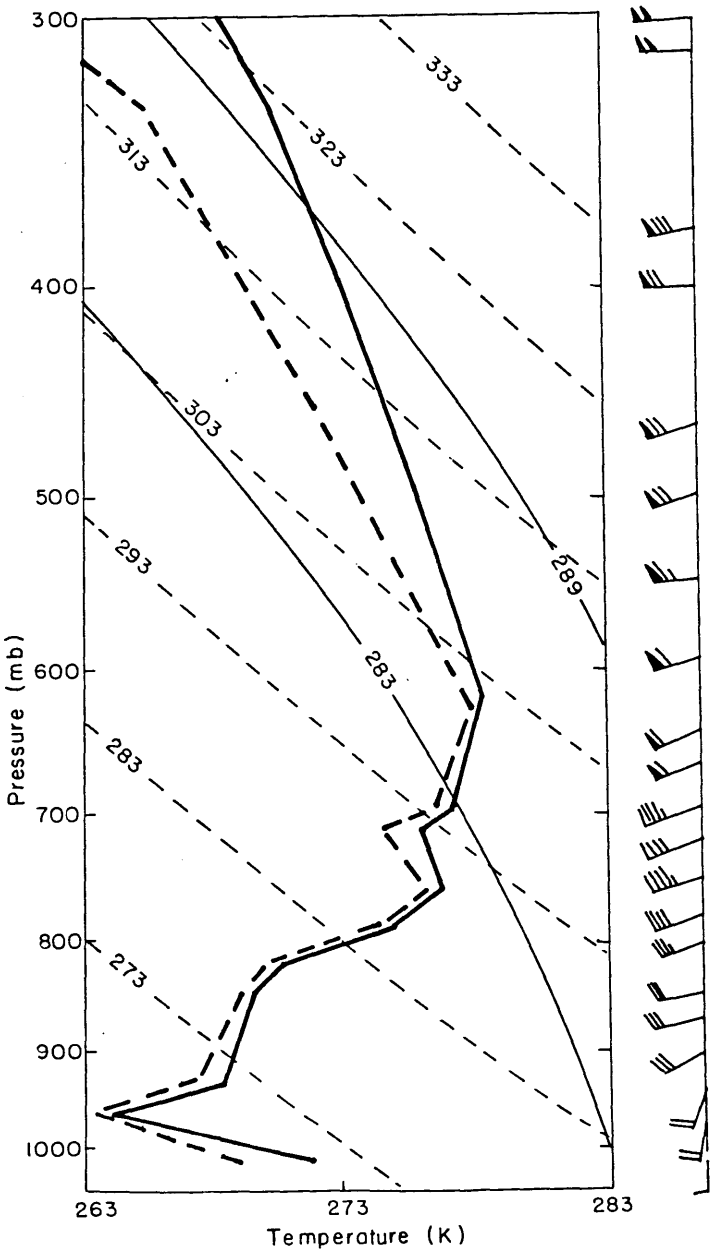

Fig. 3c Sounding for ALB at 00 GMT on 11 December 1982 plotted on a skew-T, log-p diagram. The sounding temperature and dew point temperature are shown in heavy solid and dased lines. Reference psuedo adiabats and moist adiabats are given in light solid and dashed lines. Winds are ploted on the side.

b. Analysis of Radar CAPPI Displays

In this section, the character and behavior of the bands are illustrated with radar CAPPI displays. Although reproductions of these displays do not indicate the features' continuity in time, they do show preferred regions of growth, wavelengths, orientations, and strength of the bands. Three stages of band behavior have been identified on the basis of these factors.

The strongest and most extensive precipitation occurs in the first stage, which lasts from 23 GMT 10 December to 1130 GMT 11 December. A CAPPI display of radar reflectivity through the layer between 2.5 km to 4.0 km taken at 1040 GMT 11 December is shown in Fig. 4a.

During the first stage, there are typically three to four bands oriented toward 55° (clockwise from North). The bands are oriented about 15° to the left of the mean geostrophic shear between 850 mb and 500 mb. The average band width is 30 km and the wavelength, or distance between the bands, is about 80 km. At irregular intervals, one or more of the bands breaks up into two to four smaller bands oriented at various angles to the original band axis. In some instances there is a suggestion of waviness in a band before it breaks up. Twenty to forty minutes after the

Fig. 4a stage 1, taken at 1040 GMT

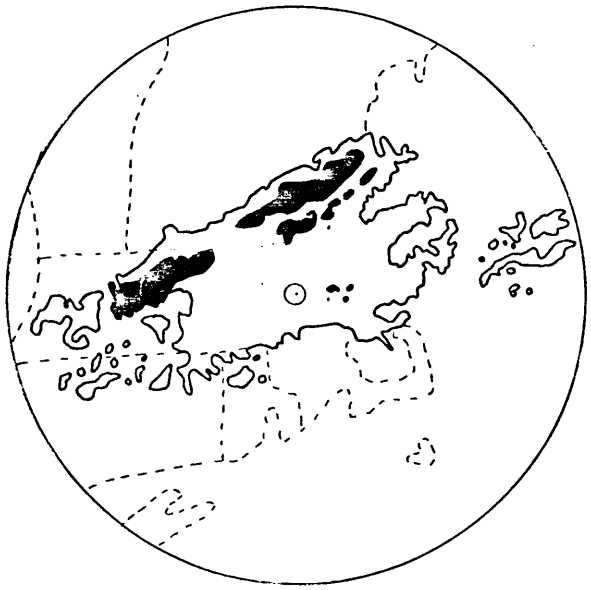

Fig. 4b stage 2, taken at 1325 GMT

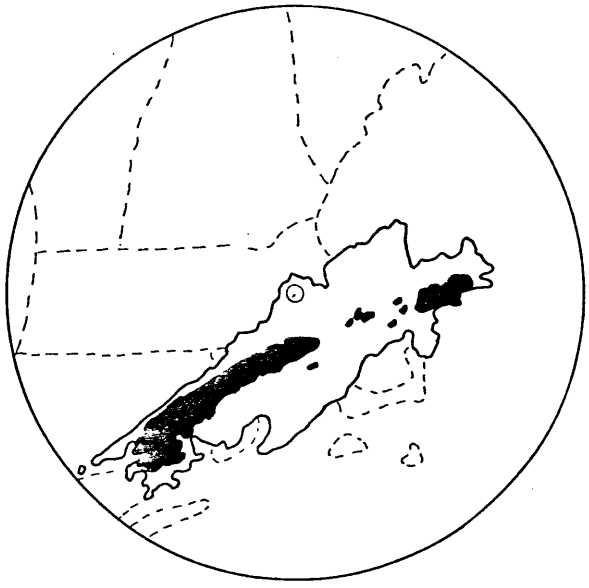

Fig. 4c stage 3, taken at 1822 GMT

Fig. 4 CAPPI displays of radar reflectivity through the layer between 2.5 and 4.0 km. Solid lines show contours of 0 dbZ. regions with dbZ>10 are shaded.

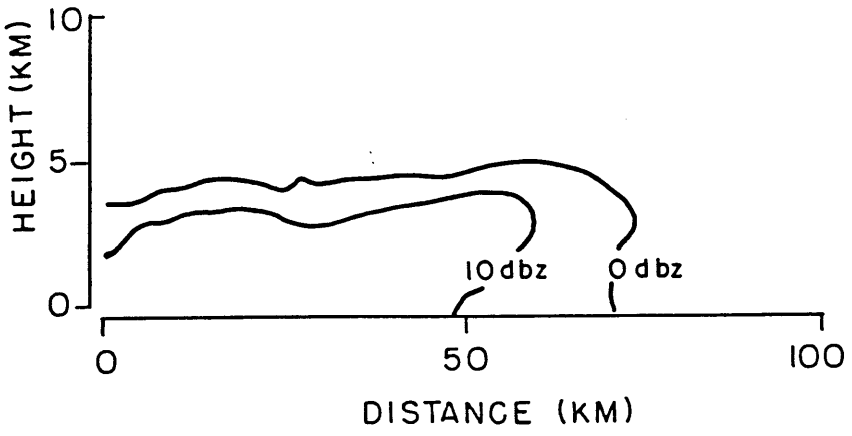

Fig. 4d RHI display of radar reflectivity taken at 953 GMT toward 140°.

break-up, one of the smaller bands rotates to 55° while the other bands decay. It is speculated that this behavior represents an instability in the bands themselves. Consideration of this phenomenon is beyond the scope of this paper. It is interesting that the original configuration is sufficiently robust that it is reestablished after a break-up.

During stage two, there is no precipitation along the south shore of Massachusetts, in Rhode Island, or in western Connecticut. The bands are weaker than in stage one. At 12 GMT, the onset of stage two is signaled by a single band extending southeastward toward 55° from the New Hampshire coast, as shown at 1202 GMT in Fig. 4b. The band is about 45 km wide. An hour later, the band splits into two parallel bands with widths of 15 km, separated by 25 km. At 1345 GMT the bands split into four bands which rapidly decay.

There is little precipitation between 1345 GMT and 1737 GMT. During stage three, the bands form in southern New England but not northern New England. The bands in stage three are about as strong as those in stage two. Stage three begins at 1737 GMT (Fig. 4c) when a band moves into the radar range toward the area between MIT and CHH. The single band, of width 20 km, decays after an hour. Another band forms to its north at the same time. During stage three the band is also oriented toward 55°-60°. By 1940 GMT, the storm moves out of New England.

Fig. 4d shows an RHI (Range Height Indicator) taken toward 140° at 953 GMT. The RHI shows that the top of the reflectivity is at about 5 km and that the band width is about 75 km.

c. Analysis of VVP time-height cross sections

Average wind velocity and divergence are computed over a 30 km radius cylinder, using Waldtuefel and Corbin's (1979) VVP technique. Vertical velocities are calculated by integrating horizontal divergence. Time-height cross sections of radar reflectivity and vertical velocity are shown in Figs. 5a-b.

The maximum vertical velocity calculated is .3 ms^{-1} at 4 GMT, 1015 GMT and 12 GMT. The maximum downward velocity is -.5 ms^{-1} at 19 GMT. The vertical velocity at times when there are no bands present is about .05 ms^{-1}. As illustrated in Fig. 4, bands generally are not centered over the radar. Because of the coarse resolution, the vertical velocities calculated are probably less than actual maximum updrafts in the bands.

The maxima in convergence (not shown) are between 1 km and 2 km and the maxima in reflectivity are slightly higher. Thus the VVP calculations suggest that the base of the band circulations is about 1.5 km.

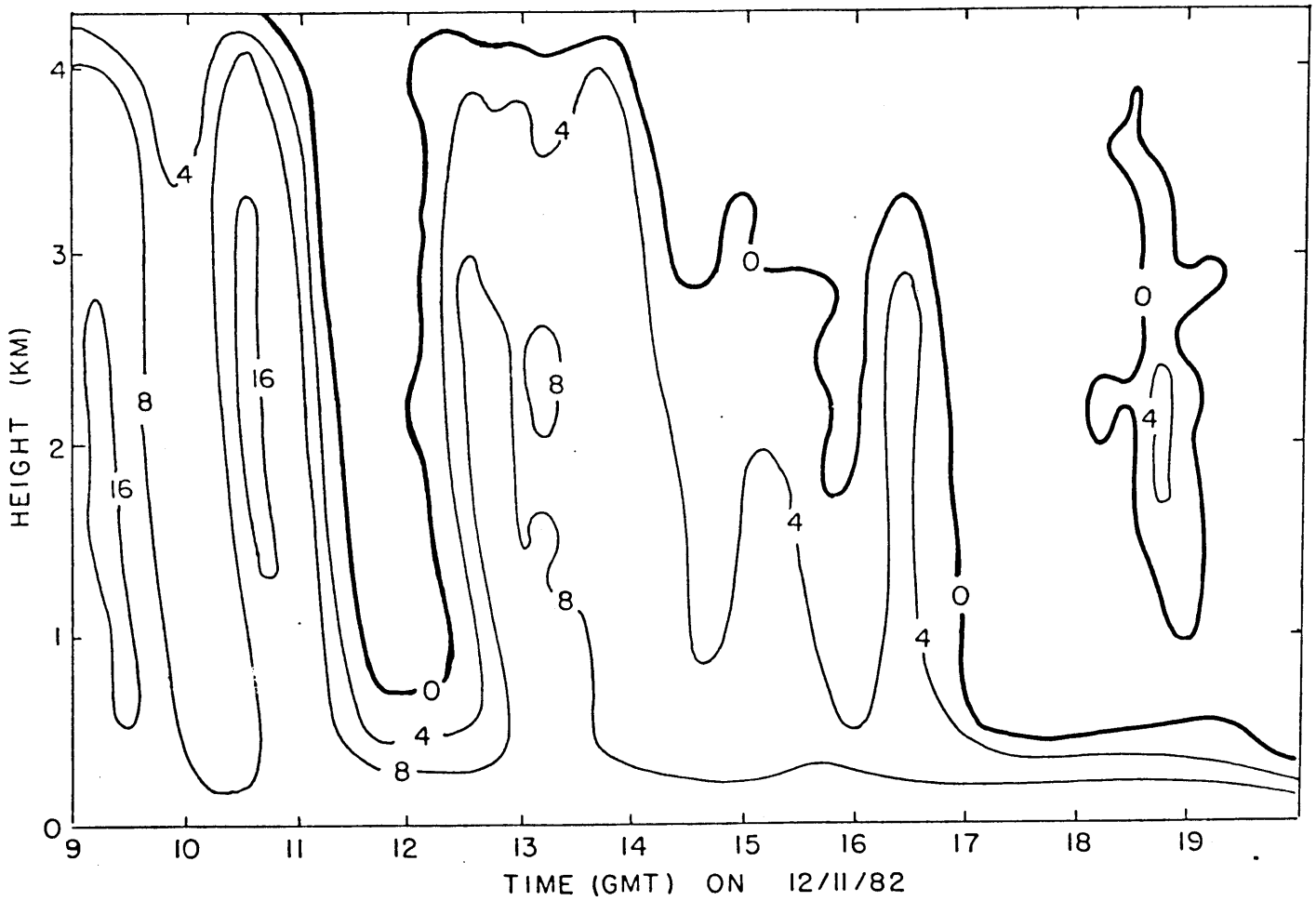

Fig. 5a average reflectivity in dB(Z)

Fig. 5 VVP time-height cross sections between 9 GMT and 20 GMT.

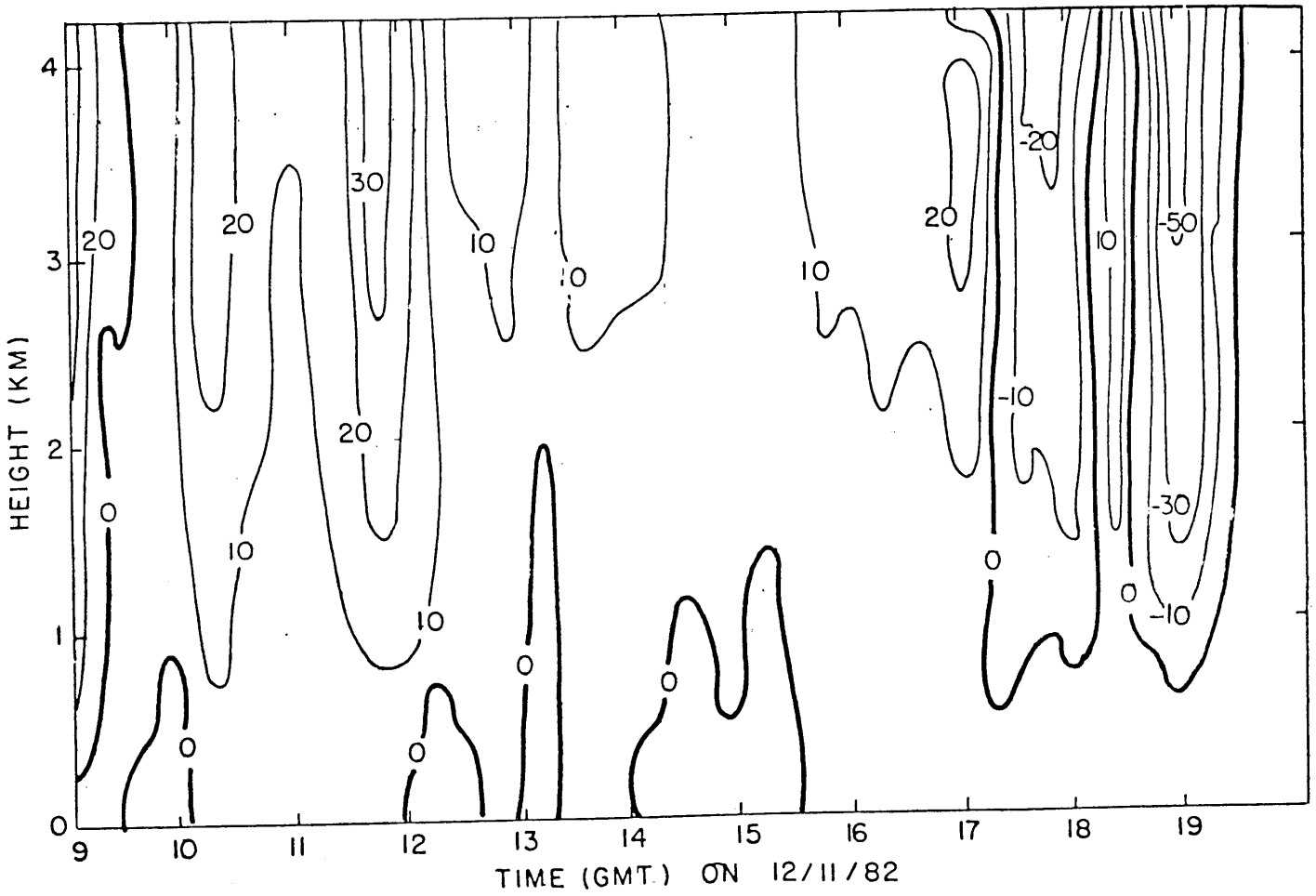

Fig. 5b vertical velocity from integrated divergence in cms^{-1}

d. Band Pass Analysis

The band pass analysis is presented in subjectively contoured cross sections which illustrate the airflow and moisture distribution in a plane perpendicular to the band. The x-coordinate runs perpendicular to the band, is oriented at 145° and increases toward warmer air. The y-coordinate is oriented along the band, toward 55°. Schematics showing the flight paths and the bands as observed on the MIT radar are given in Figs. 6a-b.

Figs. 7a-b show contours of reflectivity (Z) measured by a 200Y probe, a one-dimensional optical array probe which sizes and counts water and ice particles with diameters between 300 μm and 4500 μm. Reflectivity provides a measure of precipitation particle concentration. The airplane measurement calibrations assume that the precipitation is rain. Rain is approximately five times more reflective than the snow which was actually encountered. The reflectivities given in Figs. 7a-b are therefore approximately five times greater than values which would be recorded by a radar. The contours of high reflectivity are taken as an indication of the band location within the cross section. In the morning flight, the band is wider than the flight legs. In the afternoon flight, the band is located between 0 km and 30 km

Fig. 6a

1230 GMT flight

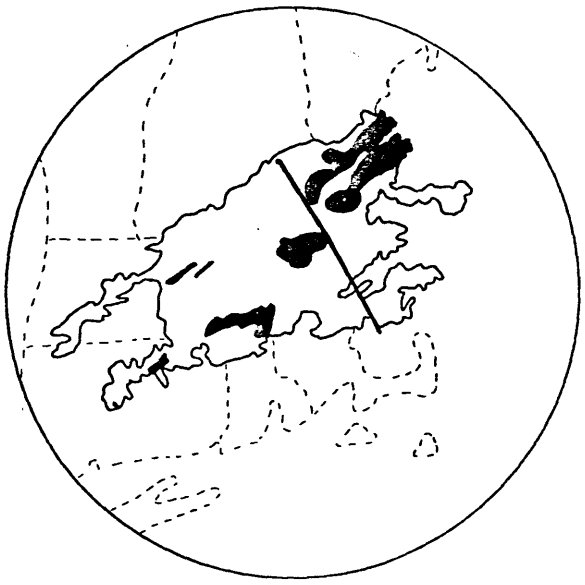

Fig. 6b

1830 GMT flight

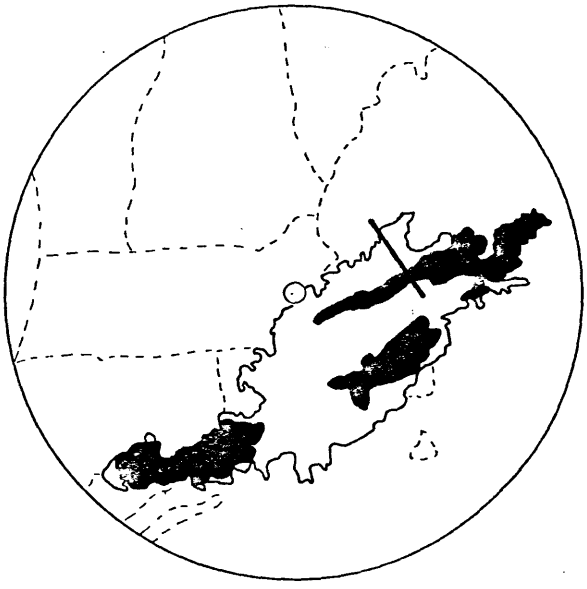

Fig. 6 Schematics of band passes showing flight legs superimposed on radar CAPPI display.

Fig. 7 Band pass cross sections. Ordinate shows height in km. Abscissa shows distance across the band in km.

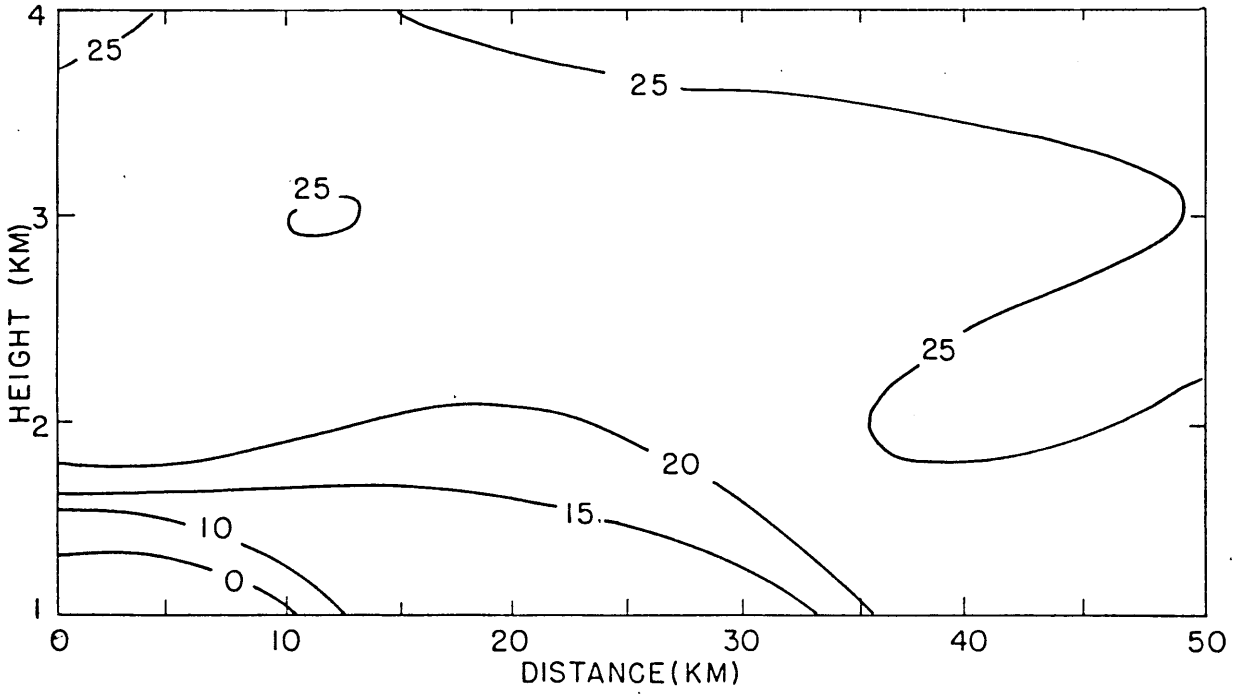

Fig. 7a reflectivity in dB(Z) for 1230 GMT flight

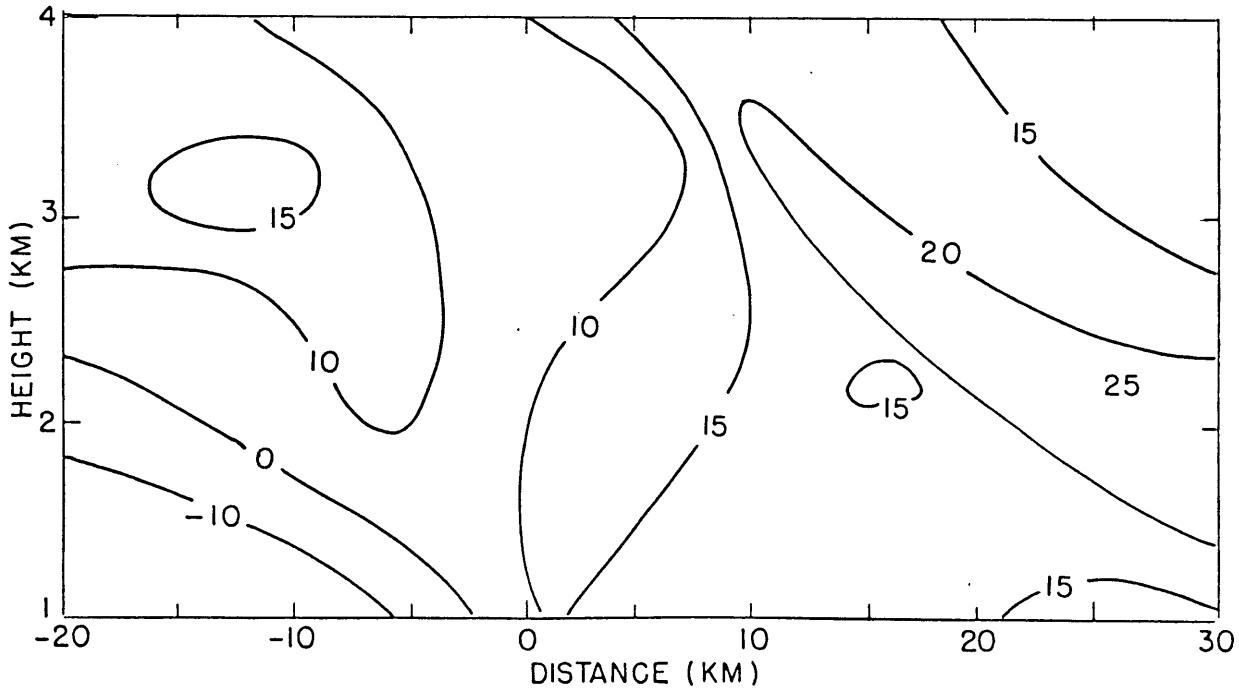

Fig. 7b as if Fig. 7a except for 1830 GMT flight

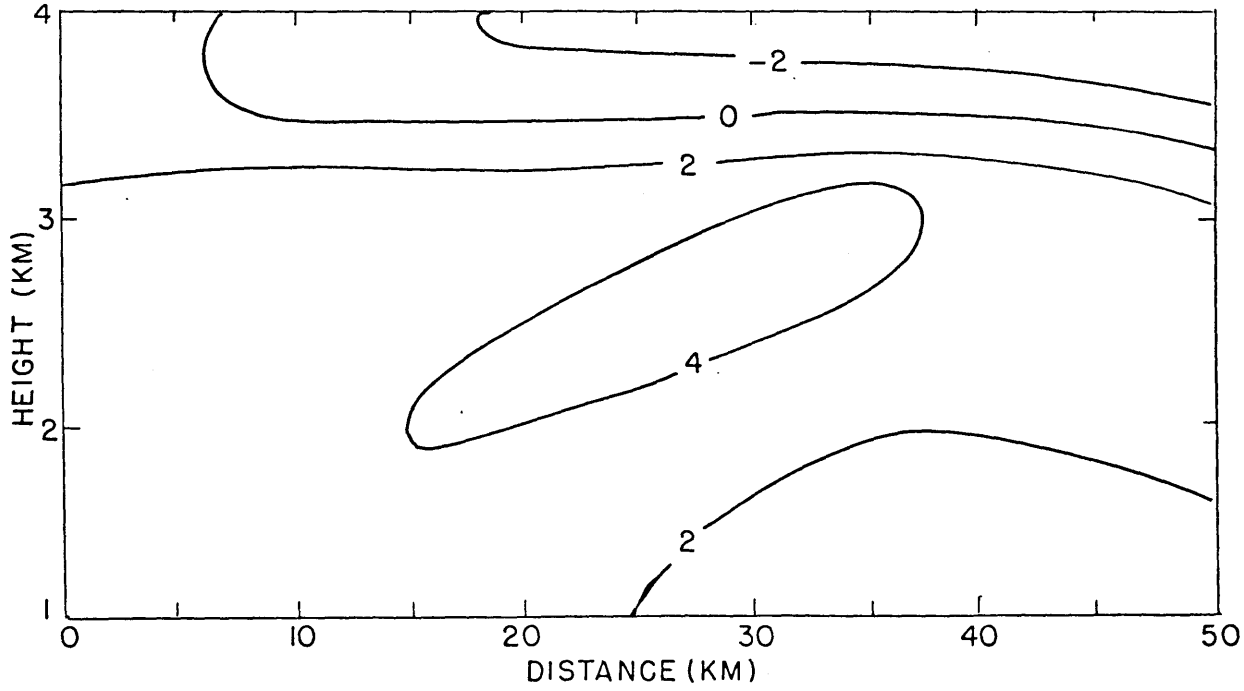

Fig. 7c band relative cross band velocity, u, in ms^{-1} for 1230 GMT flight

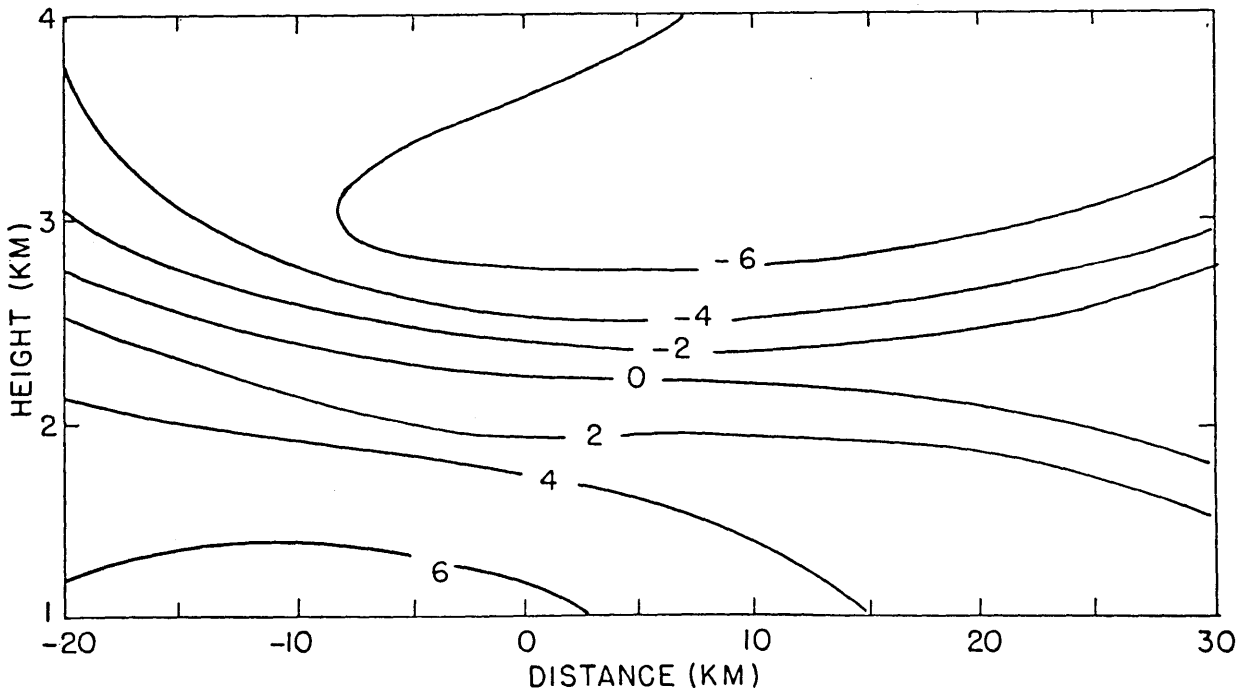

Fig. 7d as in Fig. 7c except for 1830 GMT flight

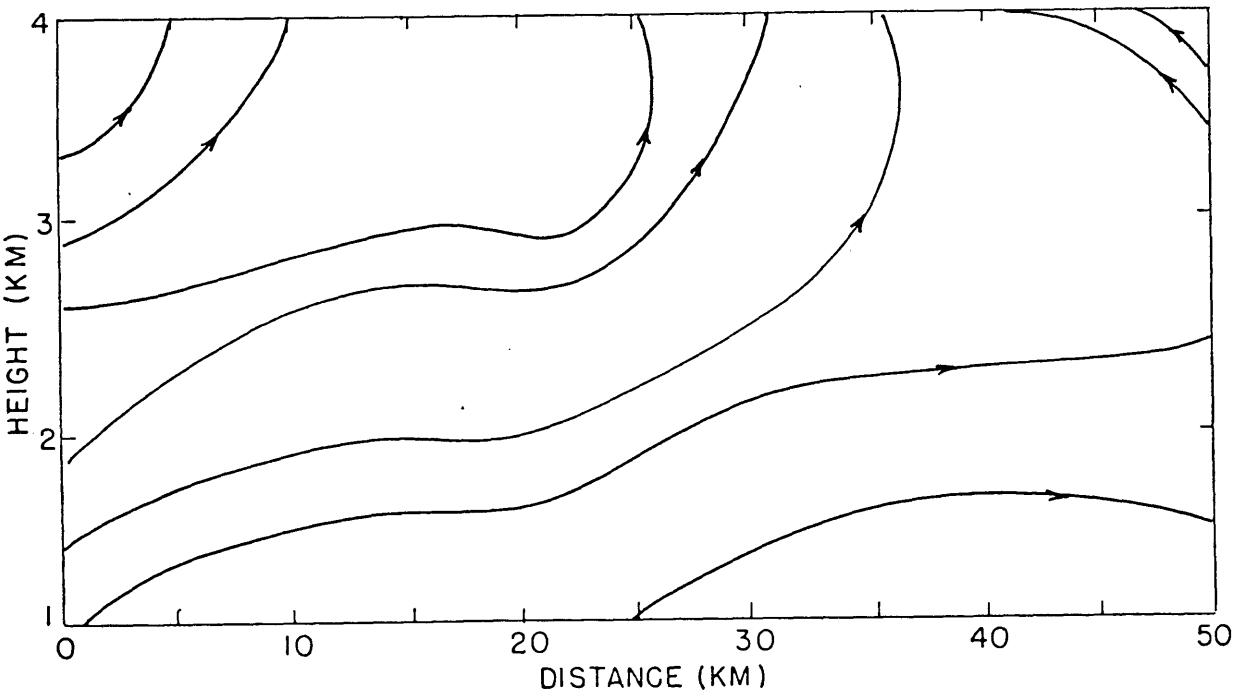

Fig. 7e band relative streamlines, drawn every 2×10^{-5} $m^2 s^{-1}$ for 1230 GMT flight

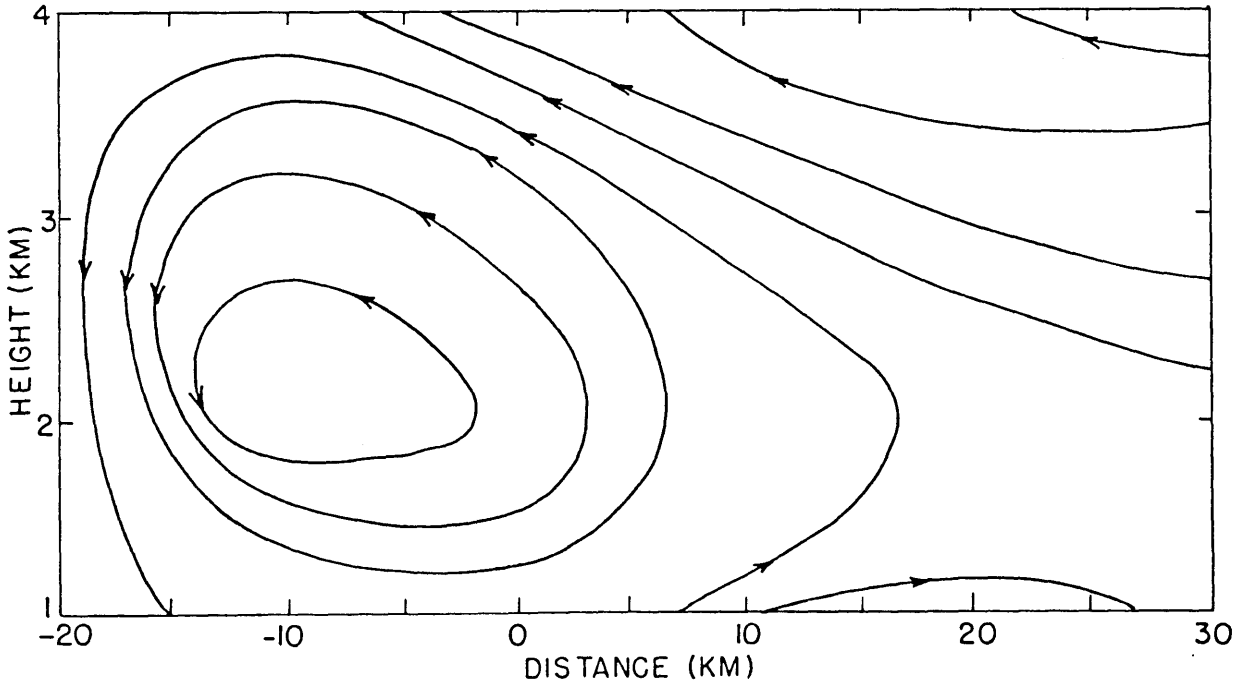

Fig. 7f as in Fig. 7e except for 1830 GMT flight

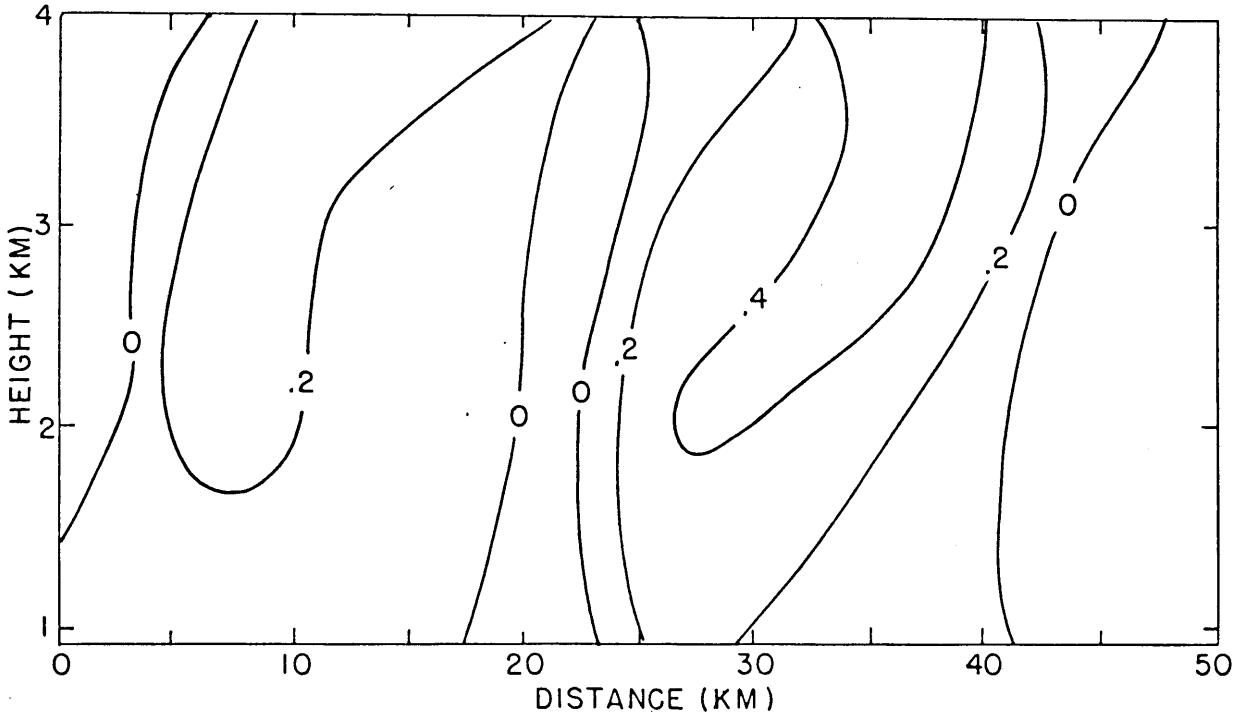

Fig. 7g vertical velocity, w, in ms^{-1} for 1230 GMT flight

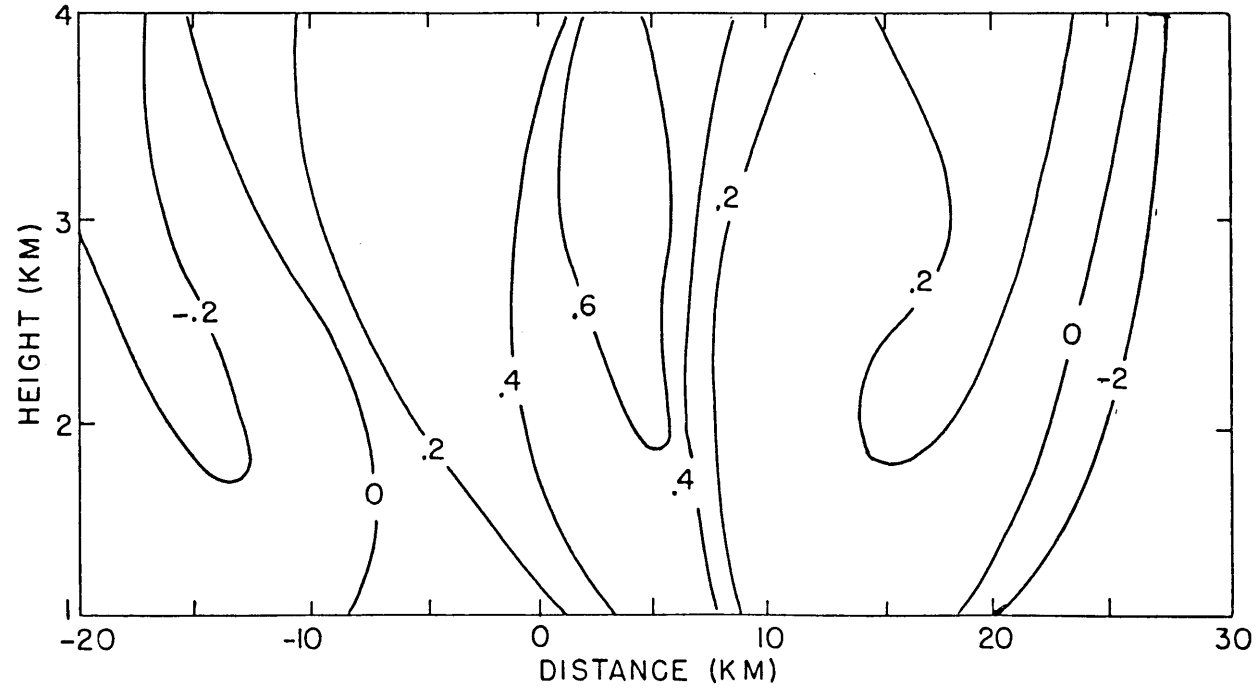

Fig. 7h as in Fig. 7g except for 1830 GMT flight

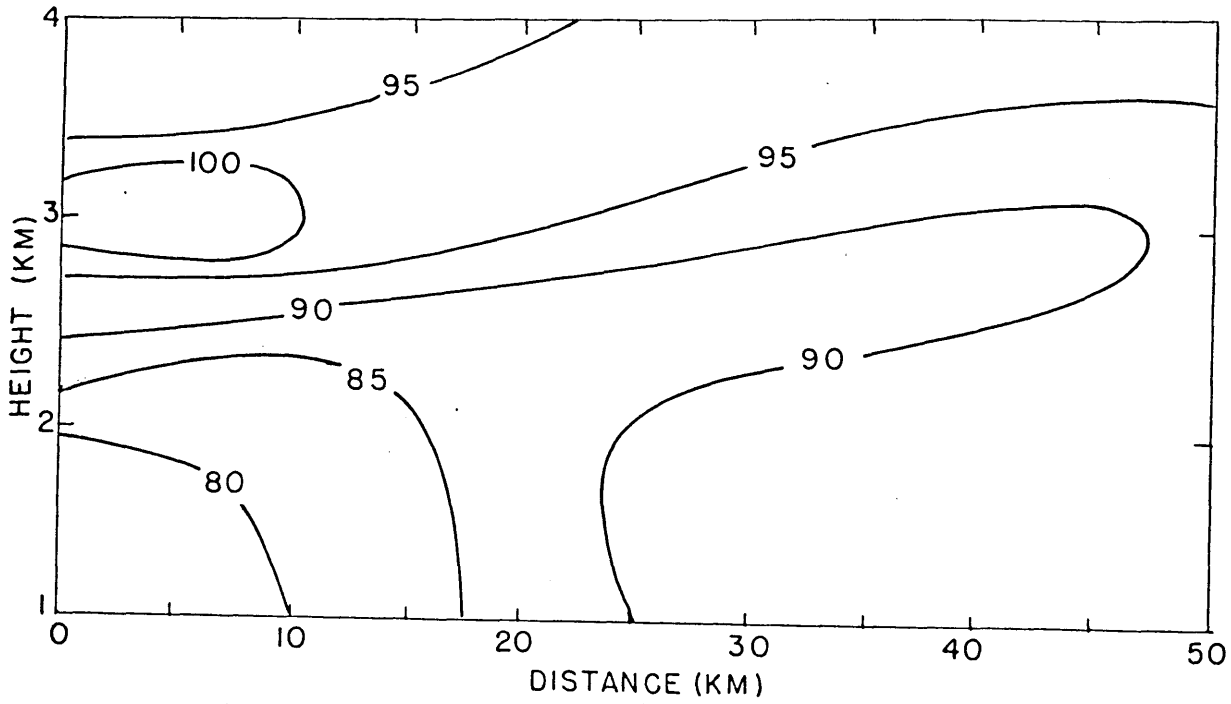

Fig. 7i relative humidity, in percent, for 1230 GMT flight

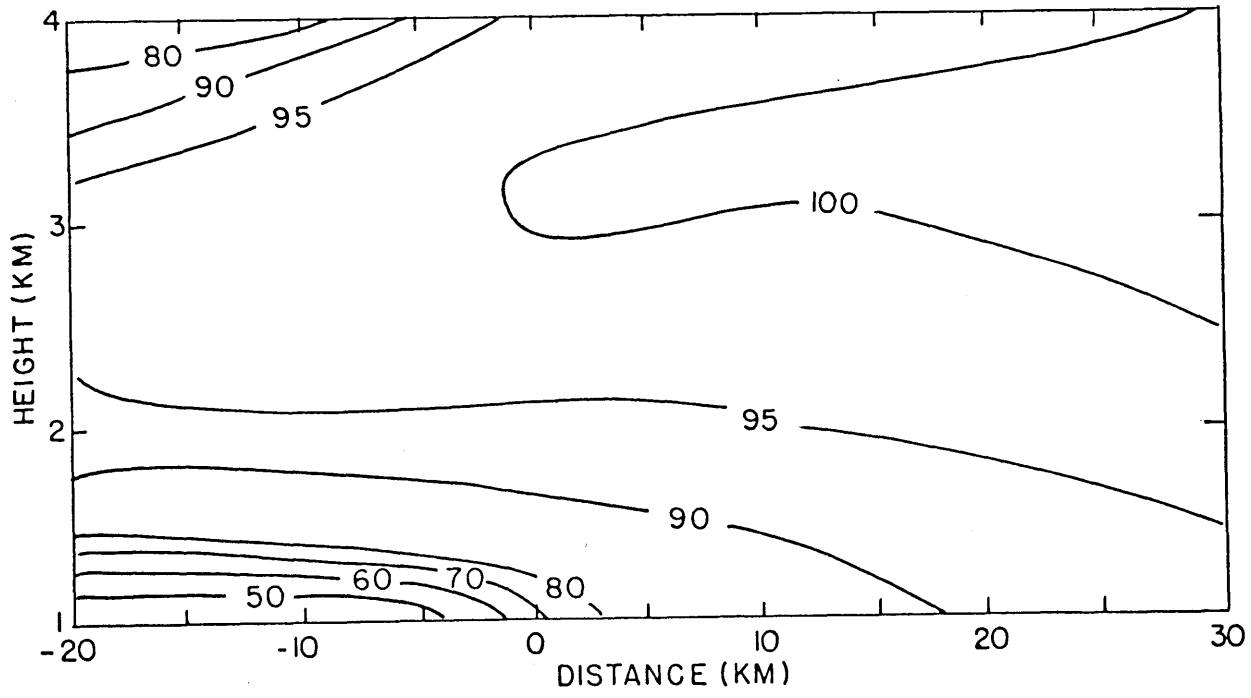

Fig. 7j as in Fig. 7i except for 1830 GMT flight

on the x-axis. The band locations indicated by aircraft reflectivity measurements agree with those indicated by the MIT radar (Fig. 6). It should be noted that the circulation associated with the band is probably wider than the band itself. Precipitation and cloud droplets grow only in an updraft so downdraft regions may not be visible on the radar.

Figs. 7c-d show isopleths of u, the cross band velocity relative to the band. In both flights the cross band wind is toward warm air at low levels and toward cold air at upper levels.

Band-relative streamlines and vertical velocities are calculated by assuming that variations along the band are small. The horizontal components of divergence, $\partial u/\partial x$ and $\partial v/\partial y$, are estimated at 00 GMT and 12 GMT with upper level winds from PWM, CHH, and YQI (Yarmouth, Nova Scotia). The u and v velocities refer respectively to the across and along band winds as defined above. The magnitude of $\partial v/\partial y$ is at most one-seventh the magnitude of $\partial u/\partial x$. The assumption of small $\partial v/\partial y$ appears to be justified at upper levels. The magnitudes of $\partial u/\partial x$ and $\partial v/\partial y$ are estimated over the ocean at 12 GMT and 18 GMT with surface winds from BOS, PSM (Portsmouth N. H.), and Buoy 44005. At both times, $\partial u/\partial x$ and $\partial v/\partial y$ are less than 10^{-5} s^{-1}. It is also assumed that the

fields of u shown in Figs. 7c-d represent a synchronous set of observations. This assumption is not strictly valid, as the flights each lasted about an hour and a half.

The band relative stream function Ψ, is defined as

$$\partial\Psi/\partial z = -u, \quad \partial\Psi/\partial x = w, \text{ with } \Psi=0 \text{ at } z=0. \tag{1}$$

If $\partial v/\partial y = 0$, and $d(\ln\rho)/dt \ll \nabla\cdot v$, Ψ satisfies mass continuity. Contours of Ψ and w, calculated with finite differences, are shown in Figs. 7e-h. In both flights, (Figs. 7e-f) the slope of the streamlines in the upward branch of the circulation is about 1/30. Sanders (personal communication, 1984) also found streamline slopes of 1/30 in his study of a banded snow storm on 11-12 February 1983. In the afternoon (Fig. 7f), the streamlines show a closed roll circulation. The downdraft is almost vertical. The upward branch of the circulation occurs in the region of high reflectivity between 5 km and 25 km. There is also a reflectivity maximum at x = -5 km, in the downward branch of the circulation. It is speculated that this maximum is due to snow falling from a sloped updraft above the cross section. The reflectivity of the morning flight (Fig. 7e) is strong but fairly featureless. Such a pattern suggests a smooth updraft as indicated by the streamlines. It seems likely that the circulation in the morning experiment is also

a roll but that the flight legs were not long enough to observe the downward branch. It is apparent in both flights that the circulations extend above four kilometers.

The updraft strengths (Figs. 7g-h) in the morning and afternoon flights are .4 ms^{-1} and .6 ms^{-1} respectively. These values agree well with those calculated from Doppler radar velocities. The strongest convergence is at 2 km in the morning flight and at 1 km in the afternoon flight. The base of the updrafts is estimated to occur at altitudes between 1 km and 2 km, as found in the Doppler velocity analysis.

Figs. 7i-j show relative humidity. In both cases the air is saturated (relative humidity greater than 95%) in the updrafts. There is a region of very low relative humidity in the lower left corner of both cross sections. In the afternoon flight, this dry region corresponds to the descending branch of the circulation. The air in this region on the morning flight cross section probably experienced a recent descent as well. The reflectivities (Figs. 7a-b) in the lower left corners of the cross sections are also low.

e. Summary of Band Characteristics

The bands developed in a large scale environment characterized by strong vertical shear. The geostrophic

shear backed with height between 500 mb and 850 mb over New England. A sounding showed extensive saturation, high stability at low levels, and lower stability at upper levels. Very small synoptic-scale vertical velocity was inferred from the synoptic maps. Strong ageostrophy was observed on these maps. Warm fronts were observed on the surface maps.

Gross features of the bands were inferred from series of CAPPI displays. The bands were quasi-linear in shape and were oriented about 15° to the left of the mean geostrophic shear. The bands moved slowly. The maximum convergence was at about 1.5 km. The reflectivity tops observed on the radar were at about 5 km. Multiple bands were frequently observed. The bands were 20 km to 50 km wide, formed in 20 to 40 minutes and lasted 3 to 6 hours. There was time-dependent behavior in the bands.

The structure and circulation of the bands were observed with airplane band passes. The afternoon flight in particular showed a sloped roll circulation with an updraft slope of 1/30 and a vertical downdraft. The updrafts were saturated, and there was low relative humidity in the downdrafts. The vertical velocity was .6 ms^{-1} in the bands and .05 ms^{-1} between the bands.

IV. ROLE OF SYMMETRIC INSTABILITY

a. The Parcel Model of Moist Symmetric Instability

Bennetts and Hoskins (1979) and Emanuel (1979) have suggested that some bands which form in layers of stable or neutral thermal stratification and are imbedded in regions of large scale ascent may be caused by symmetric instability. Symmetric instability is manifested in sloped, two-dimensional, mesoscale rolls aligned with the geostrophic shear. The parcel description of moist symmetric instability below closely follows Emanuel (1983b,d).

Symmetric instability arises when perturbations in the density and velocity fields are unstable to the combined centrifugal and gravitational force. The atmosphere may be convectively and inertially stable and yet symmetrically unstable.

We will consider a base state in which a steady, purely zonal flow is in geostrophic balance. Then the potential temperature is a function only of x and z. The equations for the base state zonal geostrophic velocity, v_g, and virtual potential temperature, θ_v, are

$$dv_g/dt = 0 \tag{2}$$

$$f(dv_g/dz) = (g/\theta_{v0})\partial\theta_v/\partial x \tag{3}$$

where the subscript "g" denotes the geostrophically and hydrostatically balanced base state.

Suppose a tubular parcel of fluid, extending infinitely in the y direction is displaced in the x-z plane. The displacement is assumed to proceed slowly so that fields of v_g, θ_v, and pressure are undisturbed. The perturbation equations are

$$dv_p/dt = -fu_p \tag{4}$$

$$du_p/dt = f(v_p - v_g) \tag{5}$$

$$dw_p/dt = g/\theta_{v0}(\theta_{vp} - \theta_v) \tag{6}$$

where the subscript "p" refers to the parcel. It can be shown that a pseudo-angular momentum, M, defined as

$$M = v + fx \tag{7}$$

is conserved following the parcel, if the vertical shear is unidirectional. Eq. (5) can be written

$$du_p/dt = f(M_p - M_g) \qquad (8)$$

If, after the displacement, the left-hand sides of Eqs. (6) and (8) are positive, the parcel will continue accelerating, so the displacement is unstable. An illustration of the meaning of Eqs. (6) and (8) is shown in Figs. 8a-b. M and θ increase upward and to the right in both figures so they represent gravitationally and inertially stable configurations. In Fig. 8a, the slope of θ is less than the slope of M. If a parcel is lifted as shown it will have lower values of M and θ than its environment. The restoring force is opposite the direction of the displacement, so the displacement is stable. In Fig. 8b, the slope of M is less than the slope of θ. A displacement with a slope intermediate between the slopes of M and θ will result in the parcel's having a lower value of M and a higher value of θ than the environment. The restoring force has a component in the direction of the displacement. Slanted displacements may be unstable if the slope of M is less than that of θ. Symmetric instability is sometimes referred to as "slantwise convection." If the environment is saturated, θ_e should be substituted for θ to account for release of latent heat. If the environment is moist but not saturated, a quantity S is

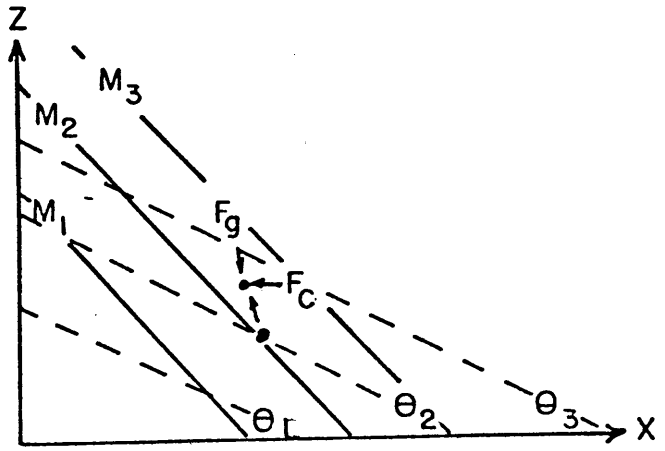

Fig. 8a Stable configuration. M surfaces are steeper than θ surfaces. A parcel lifted as shown is subject to gravitational and centrifugal restoring forces.

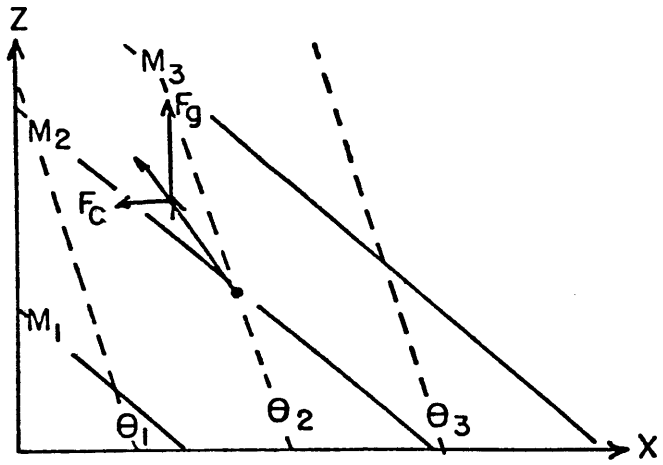

Fig. 8b Unstable configuration. θ surfaces are steeper than M surfaces. A parcel lifted as shown is subject to forces in the direction of the displacement.

Fig. 8 Schematic illustration of symmetric stability and instability. θ (dashed lines) and M (solid lines) both increase upward and to the right. The directions of the resulting gravitational (F_g) and centrifugal (F_c) are indicated.

introduced. Surfaces of S are surfaces along which the parcel has neutral buoyancy. The shape of the S surface is defined uniquely for each parcel. The parcel is lifted dry adiabatically until it reaches its lifting condensation level (LCL) and moist adiabatically above that level. Fig. 9 shows a possible configuration of M_g and S in a saturated envrironment. . Slantwise negative and positive area (SNA and SPA), the negative and positive area between the environmental and parcel temperature, are shown. The level of free convection (LFC) and level of neutral buoyancy (LNB) for slantwise convection are also indicated.

b. Slantwise Potential Energy

The potential energy available to a slantwise displacement is the path integral of the forces in eqs. (6) and (8). The potential energy, or the slantwise positive area (SPA) given by Emanuel (1983b) is

$$SPA = \int_{LFC}^{LNB} \left[f(M_p - M_g)i + \frac{g}{\theta_{v0}} (\theta_{vp} - \theta_{vg})k \right] \cdot ds \qquad (9)$$

where the LNB and LFC are the level of neutral buoyancy and the level of free convection. It can be shown that the curl of the integrand is zero. If the integrand is F then

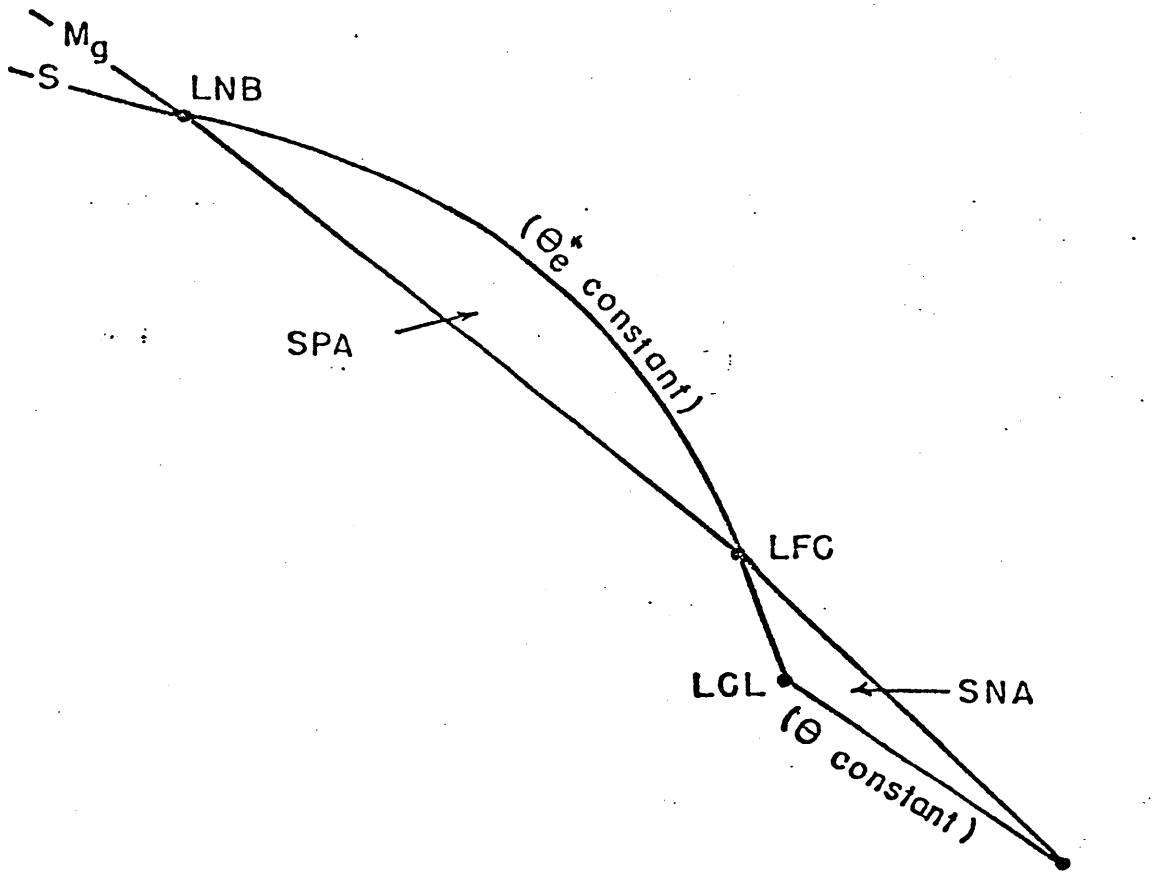

Fig. 9 Schematic illustrating a possible configuration of M_g and S surfaces for a parcel subject to slantwise convection in a saturated environment. The S surface is a contour of potential temperature below the lifting condensation level (LCL) and a contour of θ_e* above that level. θ_e* is the equivalent potential temperature a parcel at a given temperature would have if it were saturated. θ_e* is conserved only if the air is saturated. The level of free convection (LCL), the level of neutral buoyancy (LNB), slantwise negative area (SNA), and slantwise positive area (SPA) are indicated.

$$\nabla x\underset{\sim}{F} = -\hat{j}\left[\frac{\partial}{\partial z}f(M_p - M_g) - \frac{\partial}{\partial x}\frac{g}{\theta_{v0}}(\theta_{vp} - \theta_{vg})\right] \tag{10}$$

M_p and θ_{vp} are constant so

$$\nabla x\underset{\sim}{F} = -\hat{j}\left[-f\frac{\partial M_g}{\partial z} + \frac{g}{\theta_{v0}}\frac{\partial}{\partial x}\theta_{vg}\right] \tag{11}$$

$$= -\hat{j}\left[-f\frac{\partial v_g}{\partial z} + \frac{g}{\theta_{v0}}\frac{\partial}{\partial x}\theta_{vg}\right] \tag{12}$$

Eq. (12) is zero by the thermal wind relation. This result implies that the integral is path independent. If it is evaluated along an M_g surface, the first term of the integrand in eq. (9) drops out so

$$SPA = \int_{LFC}^{LNB}\int_{M_g}\left[\frac{g}{\theta_{v0}}(\theta_{vp} - \theta_{vg})\hat{k}\cdot ds\right] \tag{13}$$

SPA can be evaluated as described in Emanuel (1983a) by constructing a vertical cross section of M_g, θ, and dew point temperature (T_D) surfaces. The values of θ and T_D are read along an M_g surface, plotted on a tephigram and evaluated in the standard manner.

c. Time Rate of Change of SPA

The time rate of change of SPA is

$$\frac{d}{d\tau}SPA = \frac{d}{d\tau}\left[\int_{LFC}^{LNB}\int_{M_g}\frac{g}{\theta_{v0}}(\theta_{vp} - \theta_{va})\hat{k}\cdot ds\right] \tag{14}$$

or

$$\frac{d}{d\tau}SPA = \frac{g}{\theta_{v0}}\left[\int_{LFC}^{LNB}\int_{M_g}\left(\frac{d}{d\tau}\theta_{vp} - \frac{d}{d\tau}\theta_{va}\right)\hat{k}\cdot ds\right. \tag{15}$$

$$\left. + \frac{dz_{LNB}}{d\tau}(\theta_{vp} - \theta_{va})\Big|_{z=LNB} - \frac{dz_{LFC}}{d\tau}(\theta_{vp} - \theta_{va})\Big|_{z=LFC}\right]$$

where $d/d\tau$ is the time rate of change for a specific parcel as it is lifted along an M_g surface and the subscript "a" refers to the ambient environment. The last two terms of eq. (15) are zero because the environmental and parcel potential temperature are equal at the LFC and LNB. Eq. (14) is therefore

$$\frac{d}{d\tau}SPA = \frac{g}{\theta_{v0}}\int_{LFC}^{LNB}\int_{M_g}\left(\frac{d}{d\tau}\theta_{vp} - \frac{d}{d\tau}\theta_{va}\right)\hat{k}\cdot ds \tag{16}$$

M_g surfaces are vertical in the semi-geostrophic coordinate system described in Hoskins et. al. (1975). The time rate of change for a parcel lifted vertically in this coordinate system gives the time rate of change for a parcel lifted along an M_g surface in physical coordinates. The coordinate transformation is

$$X = x + v_g/f \tag{17a}$$

$$Y = y - u_g/f \tag{17b}$$

$$Z = z \tag{17c}$$

$$\Phi = \phi + (u_g^2 + v_g^2) \tag{17d}$$

$$T = t \tag{17e}$$

The capital letters are the new coordinate system and small letters are the physical coordinate system. ϕ is the geostrophic geopotential in physical coordinates and Φ is the semi-geostrophic geopotential. The time rate of change in semi-geostrophic coordinates is

$$\begin{aligned} d/d\tau &= \partial/\partial t + \underset{\sim}{v}_p \cdot \nabla_X \\ &= d/dt + (\underset{\sim}{v}_p - \underset{\sim}{v}_a)\cdot\nabla_X - w_a \partial/\partial Z \end{aligned} \tag{18}$$

where $\underset{\sim}{v}_a$ and w_a are the horizonatal and vertical velocities of the environment and ∇_X is the horizontal gradient operator in semi-geostrophic coordinates. Effects of friction are neglected here because the circulation base is above the surface in this case.

The parcel potential temperature is changed by radiational heating and latent heat release.

$$\frac{d}{d\tau}\theta_{vp} = \frac{Q}{C_p} - \frac{L_v}{C_p}\frac{d}{d\tau}q_s \tag{19}$$

where Q is the radiational heating per unit mass, C_p is the constant pressure heat capacity of dry air, L_v is latent heat of vaporization and q_s is the saturation mixing ratio which varies in Z. If the parcel is saturated, a linearization of the Clausius-Clapeyron equation gives

$$\frac{d}{d\tau}q_s = \frac{L_v q_s}{R_v T\theta}\frac{d}{d\tau}\theta_p \tag{20}$$

where R_v is the gas constant for water vapor and T and θ are average values of temperature and potential temperature. With this approximation, eq. (19) is

$$\frac{d}{d\tau}\theta_{vp}=\frac{Q/C_p}{1+\frac{L_v{}^2 q_s}{C_p R_v T\theta}} \tag{21}$$

Eq. (21) is valid provided the parel is saturated, as it is between the LFC and LNB. The rate of change of the environmental potential temperature is

$$\frac{d}{d\tau}\theta_{va} = \frac{Q_a}{C_p} - \frac{L_v}{C_p}\frac{d}{d\tau}q_s \tag{22}$$

Radiational heating is small except at the surface so environmental radiational heating, Q_a, can be neglected. The saturation mixing ratio of the environment is changed mainly by upward motion of the environment. If the atmosphere is saturated, eq. (22) can be written

$$\frac{d}{d\tau}\theta_{va} \approx -w_a \frac{\partial}{\partial z}\frac{L_v}{C_p}q_s \tag{23}$$

In this case, surface processes of heating and friction can be neglected because the stable boundary layer ensures that air parcels recently in contact with the surface do not reach the mid-troposphere. With this assumption and eqs. (18), (21), and (23), eq. (16) can be written

$$\frac{d}{d\tau}SPA \approx \int_{LFC}^{LNB}\left[\frac{g}{\theta_{v0}}(v_{ga} - v_{gp})\cdot\nabla_x\theta_v + w_a\frac{\partial}{\partial z}\left(\frac{g}{\theta_{v0}}\theta_e\right)\right]dz \tag{24}$$

where $\theta_e(g/\theta_{v0}) \approx \theta_v(g/\theta_{v0}) + q_s(L_v/C_p)$. The processes which can change SPA are geostrophic lapse rate advection and correlation of w and $\partial\theta_e/\partial z$. It will be shown that the former process is important in this case. Geostrophic lapse rate advection, which is given by the first term in the integrand, can be written

$$(\underset{\sim}{v}_{ga} - \underset{\sim}{v}_{gp}) \cdot \nabla\theta_a = \frac{g}{f\theta_0}(Z - Z_p)[k(\nabla\theta \times \overline{\nabla\theta})] \quad (25)$$

where

$$(\underset{\sim}{v}_{ga} - \underset{\sim}{v}_{gp}) = \hat{k} \times \frac{g}{f\theta_0}\overline{\nabla\theta}$$

through the thermal wind relation and

$$\overline{\nabla\theta} = \frac{1}{(Z - Z_p)} \int_{Z_p}^{Z} \nabla\theta dZ$$

where Z_p is the parcel level. The right hand side of eq. (25) is zero if the geostrophic shear does not turn with height and is greater than zero if it turns counterclockwise with height in the Northern Hemisphere. If eq. (25) is positive, SPA is increased because the lifted parcel encounters colder environmental temperatures.

d. Limitations of the Theory

Some of the assumptions in the derivation of the theory must be kept in mind when attempting to assess the atmosphere's susceptibility to symmetric instability. M is conserved only if the flow is unidirectional. In this case the geostrophic shear direction varies with height in some layers as discussed in chapter III. It is also assumed that the base state is in geostrophic balance and that deviations from this state are associated with the displacement. Such a picture is clearly inaccurate in this particular case. In chapter III, it is found that there is a local region of

ageostrophy above New England. The scale of the ageostrophy is intermediate between the synoptic scale and the band scale.

In this analysis three scales are considered separately. Susceptibility to mesoscale symmetric instability is evaluated assuming unidirectional, geostrophic flow by calculating M_g with the component of the geostrophic wind in the direction of 70°, the direction of the mean geostrophic shear between 500 mb and 850 mb over New England. It is assumed that since the angle of shear variation is small, dM/dt is small and that eq. (8) is a good approximation. The effect of the three-dimensionality of the large scale flow is considered only in terms of its effect on the time rate of change of SPA. The instability is evaluated using the distribution of θ_e along M_g. It is assumed that the pressure gradient balancing a displaced parcel is best represented by fv_g and that there is not a significant pressure perturbation associated with the ageostrophic winds. The ageostrophy is discussed in the section on frontogenetical forcing. Its effect is considered in terms of the effects of the sub-synoptic scale vertical velocity which it produces.

e. Evaluation of Susceptibility to Symmetric Instability

The susceptibility of the base state atmosphere to symmetric instability is evaluated by constructing a cross section perpendicular to the mean vertical shear. Fig. 1 shows the location of the cross section which is constructed from stations along the East Coast. The distance used in calculating $M_g = v_g + fx$ is the projection of the physical distance between the stations onto an axis perpendicular to the mean shear vector. The velocity v_g is the component of geostrophic velocity along the mean shear.

Figs. 10a-b show cross sections of θ_e and M_g at 00 GMT and 12 GMT. Clouds are indicated with scalloped lines. Regions of possible instability, i.e. where the M surfaces are parallel to or shallower than the θ_e surfaces, are shaded. The weather reported at surface stations, which are included on Fig. 1, is indicated below the cross sections.

Note the very stable layer which slopes from the surface at WAL (Wallops Island, VA) to about 3 km at CAR (Caribou, ME) in both cross sections. It is clearly associated with the warm fronts discussed in chapter II. There is a pocket of conditional thermal instability below the inversion at PWM at 00 GMT. The inversion caps any vertical motions which might develop in this region.

Fig. 10 Vertical cross sections across the shear. θ_e surfaces (solid lines) drawn every 5K and M_g surfaces (dashed lines) are drawn every 10 ms^{-1}. Clouds are indicated with scalloped lines and regions of potential symmetric instability are shaded. Upper air stations are indicated on the ordinate axis with large dots. Weather observed at surface stations is indicated below the axis. (✕✕ = light snow, ·· = light rain, ▽ = showers, ∞ = haze, ≡ = fog, ● = skies overcast, ◔ = skies broken)

Fig. 10a

00 GMT

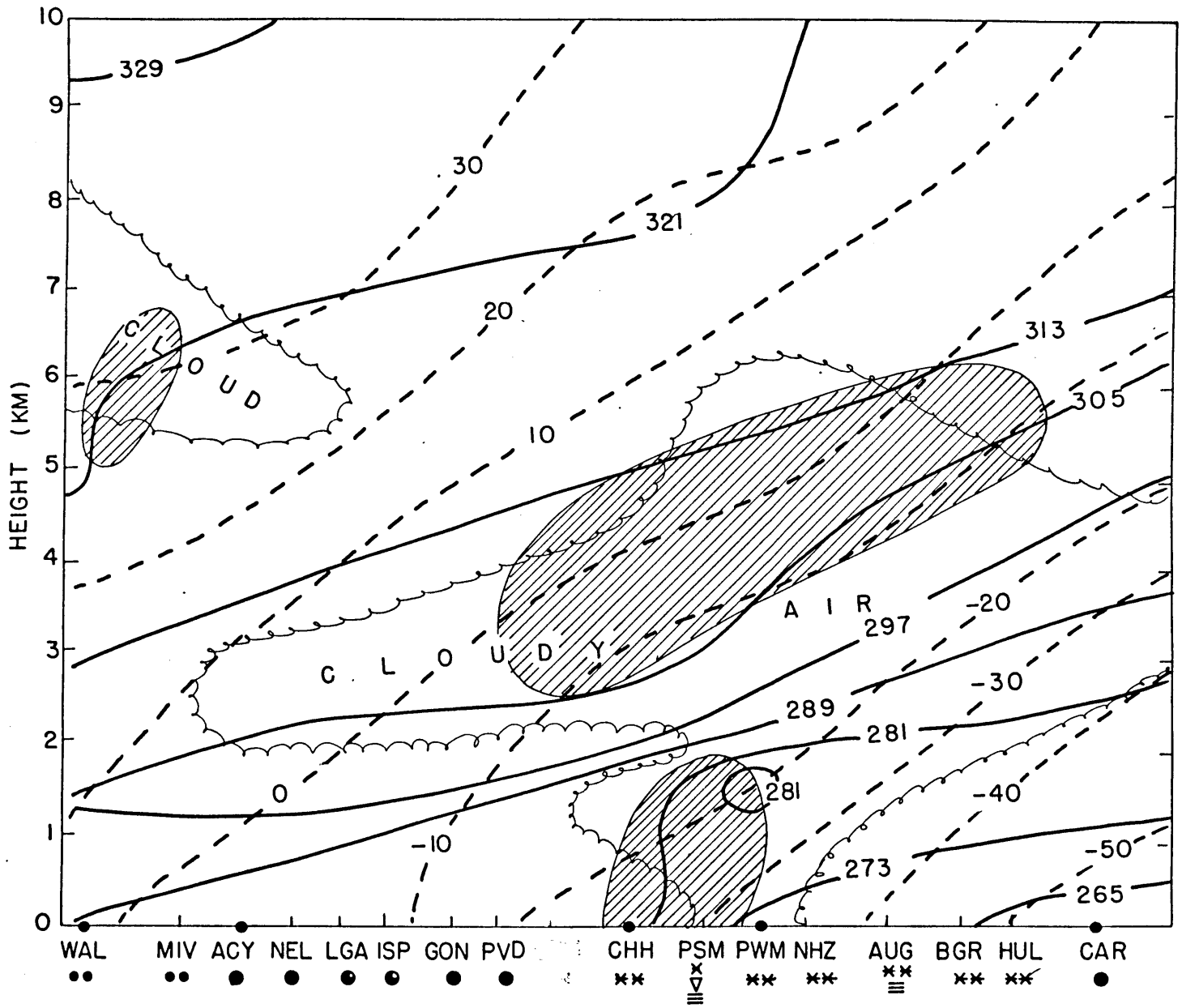

Fig. 10b

12 GMT

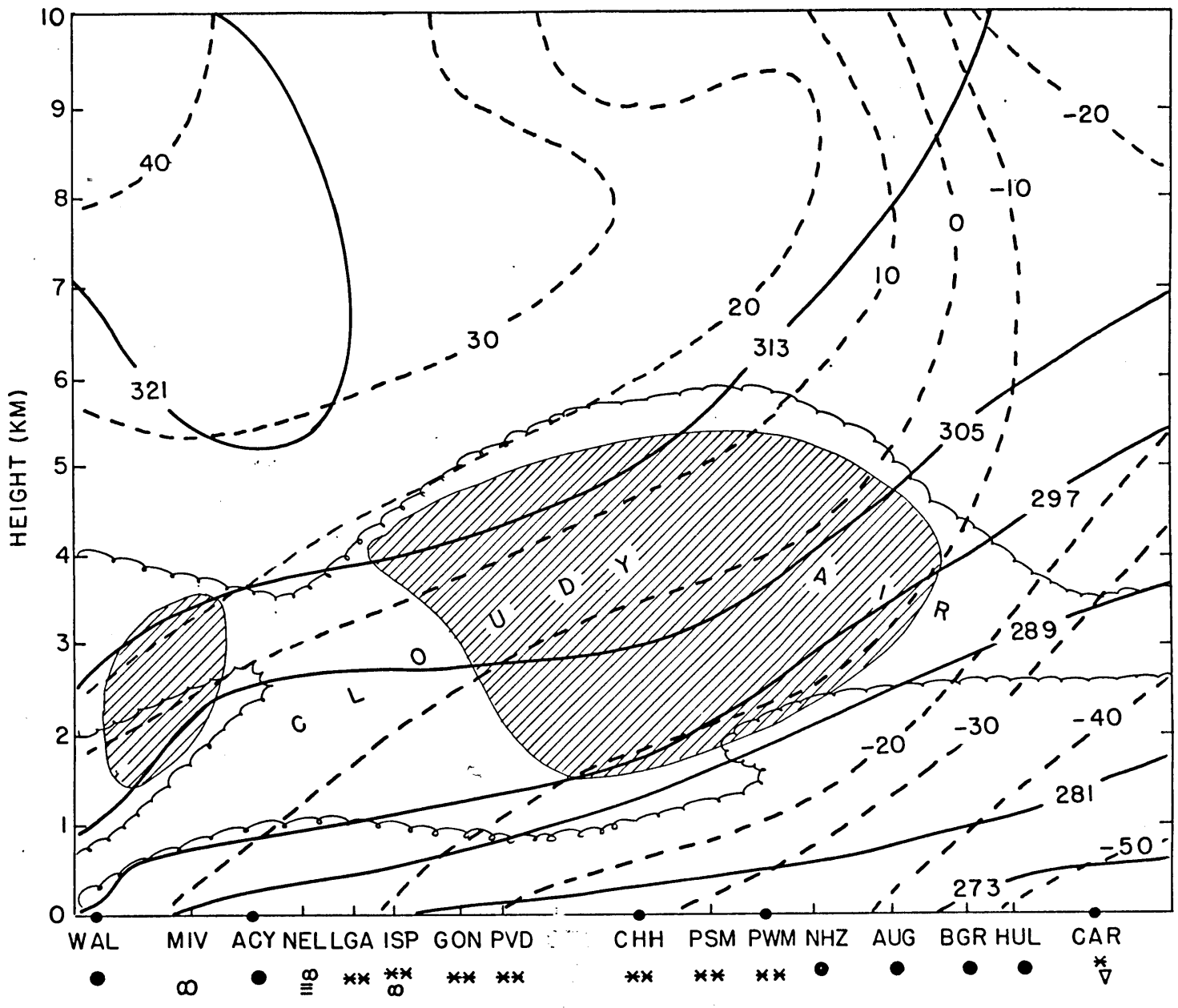

At 00 GMT, the region of possible instability slopes from 2.5 km at PVD (Providence, RI) to 5 km at HUL (Houlton, ME). The layer is about 2 km deep. At 12 GMT, the potentially unstable region extends from 4 km at ISP (Islip, NY) to 3.5 km at AUG (Augusta, ME). The thickness of the unstable layer varies from .5 km to 3 km.

Cross sections (not shown) were also constructed using the actual winds to compute M. The extent of the unstable region indicated on these cross sections was somewhat smaller than that in Fig. 10 due to the subgeostrophy of the actual winds. However, there were also thin layers of potential instability that did not appear on the geostrophic cross sections because the geostrophic winds were computed only at mandatory levels. Large changes of wind velocity within thin layers are not likely to be in geostrophic balance.

f. Evaluation of Slantwise Potential Energy

Cross sections of M, θ, and T_D (not shown) were also constructed at 00 GMT and 12 GMT. Soundings of θ and T_D are constructed along M_g = -10 m/s. The soundings were plotted on skew T, log p charts shown in Figs. 11a-b. If the most unstable parcels were lifted to achieve the greatest difference between parcel and environmental potential

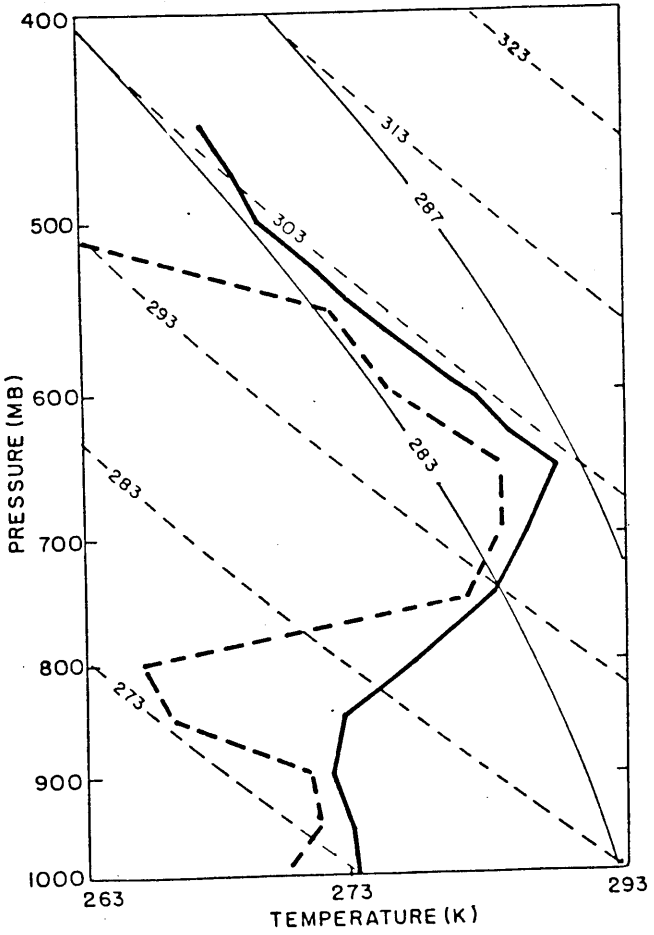

Fig. 11a 00 GMT

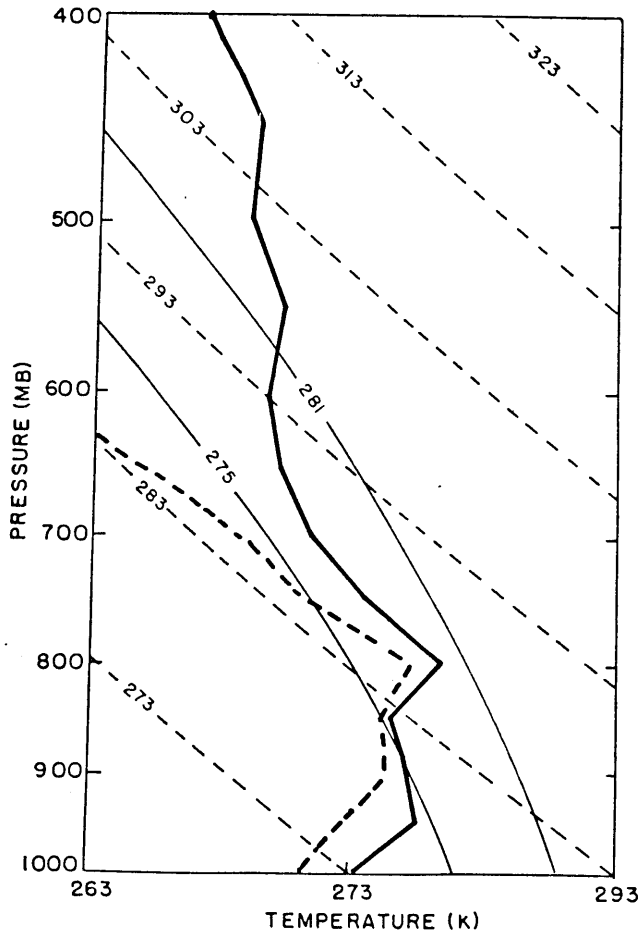

Fig. 11b 12 GMT

Fig. 11 Soundings along M = -10 ms^{-1} on skew-T, log-P diagrams. Reference dry adiabats are shown in light dashed lines. Reference pseudo-moist adiabats are shown in light solid lines. The heavy solid line and heavy dashed line are sounding temperature and dew point temperature, respectively.

temperature, there was approximately 4 degrees of buoyancy for each sounding. The vertical velocities resulting from these buoyancies can be estimated from dimensional considerations. With H≈2 km, the depth of the unstable layer, the conversion of potential energy to kinetic energy is roughly

$$KE \approx SPA \approx H\frac{g}{\theta_0}\Delta\theta \approx 2000m\frac{9.8ms^{-2}}{288K}\ 4K \approx 272\ m^2s^{-2} \qquad (26)$$

The fraction of the kinetic energy expressed as vertical motion is the slope of the M_g surface or about 1/50.

$$W \approx \frac{1}{50}\sqrt{2 \cdot KE} \approx \frac{1}{50}\sqrt{2 \cdot 272\ m^2s^{-2}} \approx .5\ ms^{-1} \qquad (27)$$

The slantwise available potential energy could yield the vertical velocities of .4 ms^{-1} to .6 ms^{-1} observed.

g. Depletion and Generation of SPA

The symmetric overturnings irreversibly convert the potential energy to kinetic energy. Irreversibilities come from precipitation, friction, and disipation. Buoyancy is released through vertical motions, so an appropriate time

scale is $T \approx W/H$. $W \approx .5\ ms^{-1}$ is an average observed updraft, and $H \approx 2$ km, the depth of the unstable layer, can be seen as a mixing length for vertical kinetic energy. The buoyancy, B is defined as $B=g/\theta_0 \Delta\theta$, where $\Delta\theta$, the difference between the parcel and environmental potential temperature, is taken to be 4 K as before.

$$\int \frac{dB}{dt} dz \approx \frac{B}{T} H \approx \frac{9.8 ms^{-2}}{288K} 4K \frac{.5 ms^{-2}}{2km} 2km \approx .07\ m^2 s^{-3} \qquad (28)$$

SPA is generated by the processes discussed above. In this case, SPA can be affected by upward motion and geostrophic lapse rate advection. The synoptic scale vertical velocity is small. The effects of the sub-synoptic scale, frontogenetically forced upward motion are discussed in the next section. There is a contribution from geostrophic lapse rate advection in this case because the geostrophic shear backed with height in some layers. Figs. 12a-b show variation of the geostrophic shear with height at CHH at 00 GMT and 12 GMT. Note that the shear backs with height between 850 mb and 500 mb at 00 GMT and between 850 mb and 300 mb at 12 GMT. The left-hand side of eq. (25) is estimated by transforming constant pressure maps into semi-geostrophic coordinates according to eq. (17). The thickness of the layer between 850 mb and 500 mb in semi-geostrophic coordinates is proportional to $\nabla\theta$. The thermal wind, which is roughly the pressure-weighted shear

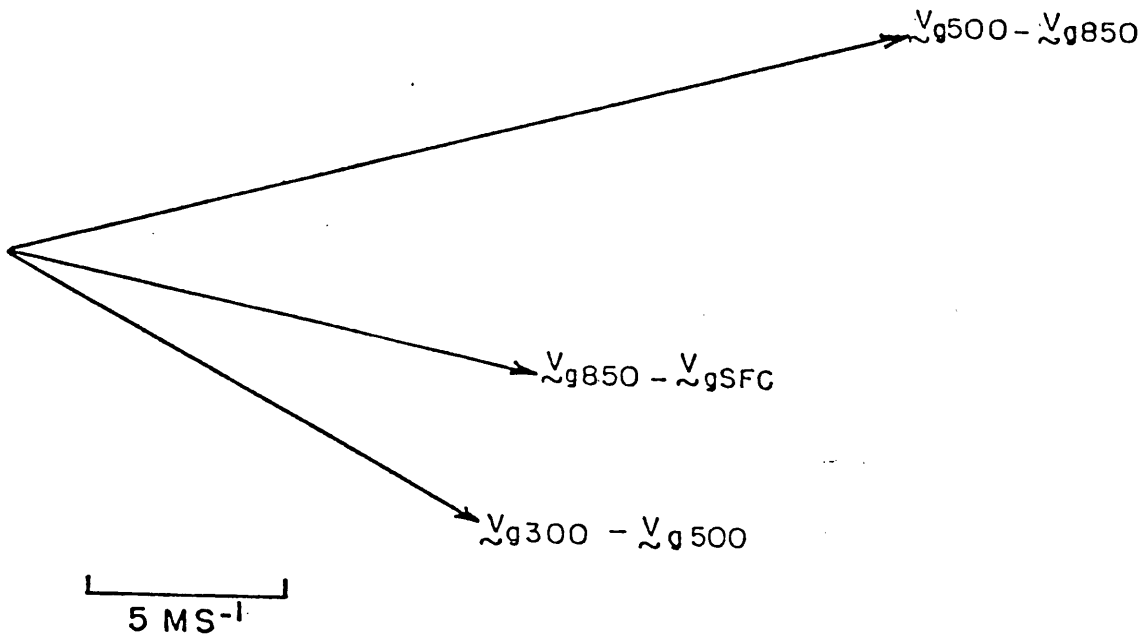

Fig. 12a 00 GMT

Fig. 12 rotation of the geostrophic shear at CHH with height

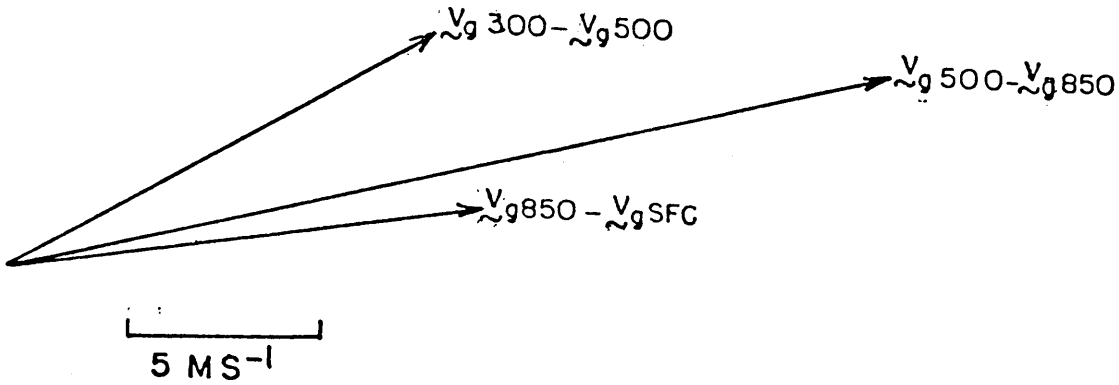

Fig. 12b 12 GMT

through the layer, flows along contours of thickness, $\nabla\Phi$. There is a positive contribution to eq. (25) in regions where the local temperature gradient along the mean thermal wind is positive. Figs. 13a-b show semi-geostrophic maps of potential temperature at 500 mb and semi-geostrophic thickness between 850 mb and 500 mb at 00 GMT and 12 GMT. The semi-geostrophic positions of the stations at 850 mb are indicated for reference. The temperature increases in the direction of the mean thermal wind in most regions in both figures. The effect of the lapse rate advection on the rate of change of SPA can be estimated dimensionally. A typical value of the vector difference $|(\underset{\sim}{v}_p-\underset{\sim}{v}_a)|$ is 25 ms^{-1}, where $\underset{\sim}{v}_p$ is evaluated at 850 mb and $\underset{\sim}{v}_a$ is evaluated at 500 mb. A typical value of $\nabla_x\theta_a$, the semi-geostrophic temperature gradient in the direction of $(\underset{\sim}{v}_p-\underset{\sim}{v}_a)$, evaluated at 500 mb, is 2.5 K in 100 km. H ≈ 4 km, the thickness of the layer between 850 mb and 500 mb.

$$\frac{dp}{dt}_{SPA} \approx \frac{g}{\theta_0}|v_{g850} - v_{g500}|\nabla_x\theta \cdot H \qquad (29)$$

$$\approx \frac{9.8ms^{-2}}{288K}\,(25ms^{-1})(2.5x10^{-5}Km^{-1})(4x10^{3}m)$$

$$\approx .09\ m^2s^{-3}$$

Fig. 13 Semi-geostrophic maps on December 11 1982. Thickness of the layer between 500 mb and 850 mb (solid lines) is drawn every 6 m^2s^2. Potential temperature at 500 mb (dashed lines) is drawn every 5K. Station locations in semi-geostrophic coordinates at 850 mb are given for reference.

Fig. 13a

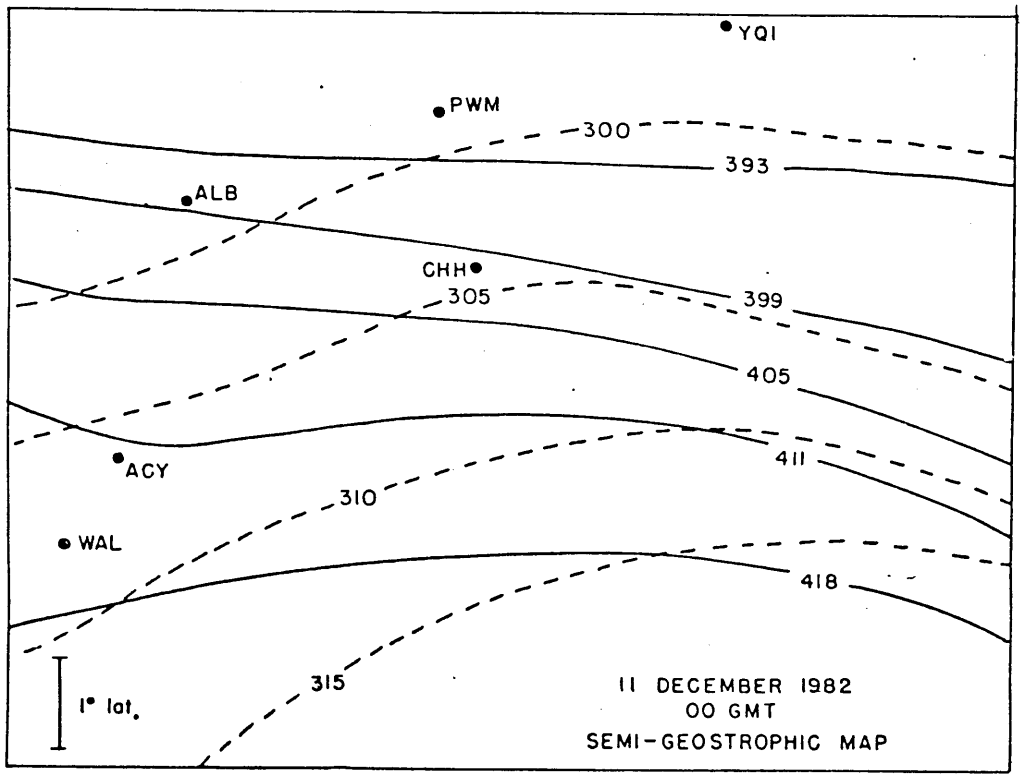

Fig. 13b

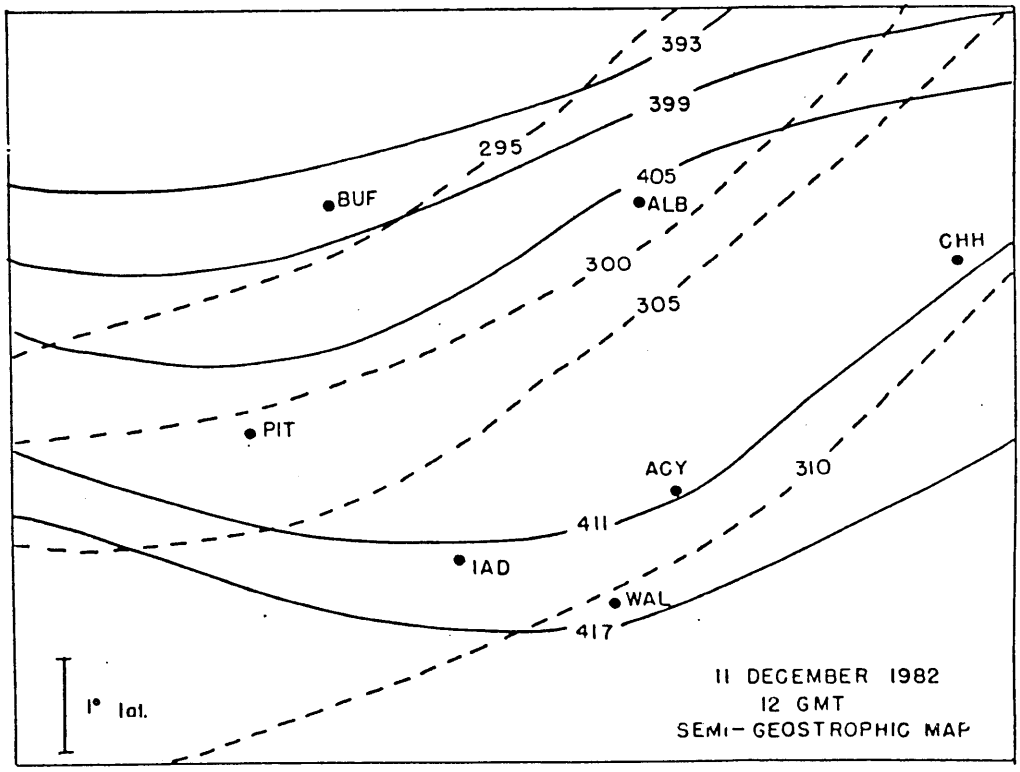

This value is of the same order of magnitude as the depletion of SPA given in eq. (28).

h. Time and Length Scales for Symmetric Instability

Emanuel (1983b,c) solved the linear stability problem for symmetric instability and derived length and time scales for the most unstable modes. In this section these scales are calculated with atmospheric parameters for this case and compared with the length and time scales actually observed.

L and σ, respectively the wavelength and linear growth rate for the most unstable mode of symmetric instability in a zonal, geostrophic and hydrostatic base state flow, are approximately

$$L \approx V_z H/f \tag{30}$$

$$\sigma^2 \approx f^2(V_z^2/N^2 - 1) \tag{31}$$

where V_z is the average vertical shear, H is the depth of the circulation, and N is the Brunt-Vaisala frequency. Typical values of these parameters during the case study are $H \approx 2$ km, $V_z \approx 10^{-2}$ s^{-1}, and $N \approx ((1/\theta_e)\partial\theta_e/\partial z) \approx 10^{-2}$ s^{-1}. With these values, eqs. (30) and (31) yield a length scale and growth rate of 200 km and 10^{-4} s^{-1},

respectively. The length scale is an order of magnitude larger than the band widths or wavelengths observed. The growth rate calculated suggests a time scale of about 3 hours, which is probably greater that the time scales observed. The bands were observed to grow smaller and weaker during the later periods of the case period. It is not obvious that this trend can be related to the parameters above. The vertical shear was generally stronger at 12 GMT than at 00 GMT. However the depth of the unstable layer was smaller in many areas at 12 GMT.

V. ROLE OF FRONTOGENETICAL FORCING

Situations which favor symmetric instability are also likely to be frontogenetically active. Large vertical shears are usually associated with deep troughs. It is well known that baroclinic waves can produce fronts (see e.g. Hoskins and West, 1979; Heckley and Hoskins, 1982). Vertical motions and ageostrophy accompany frontal circulations and complicate the picture of the base state. It is becoming clear that frontogenesis and symmetric instability are frequently related. Sanders (personal communication, 1984) found that both were active in the "megalopolitan snowstorm" of 11-12 February 1983. Emanuel (personal communication, 1984) has considered frontogenesis in a symmetrically neutral base state and found substantial modifications to the symmetrically stable case.

a. Frontogenetical Forcing of Upward Motion

The rate of frontogenesis is given by

$$-\frac{d}{dt}\nabla\theta = \nabla\underset{\sim}{v}_2\cdot\nabla\theta + \nabla w\cdot\frac{\partial\theta}{\partial z} - \nabla\frac{d\theta}{dt} \tag{32}$$

where $\underset{\sim}{v}_2$ is the horizontal wind. The first term on the right hand side describes confluent frontogenesis which gives the increase in temperature gradient due to differential advection of the isotherms. Large temperature gradients can be formed by deformation fields (see e. g. Stone, 1966; Williams, 1968). The magnitude of the deformation and the axis of dilatation, ϕ_d, are given by

$$\left|DEF\right| = \left[\left(\frac{\partial u}{\partial x} - \frac{\partial v}{\partial y}\right)^2 + \left(\frac{\partial v}{\partial x} + \frac{\partial u}{\partial y}\right)^2\right]^{.5} \tag{33}$$

$$\phi_d = \tan^{-1}\left[\frac{\left(\frac{\partial v}{\partial x} + \frac{\partial u}{\partial y}\right)}{\left(\frac{\partial u}{\partial x} - \frac{\partial v}{\partial y}\right)}\right] \tag{34}$$

where ϕ_d is measured clockwise from the x-axis. The dilatation axis gives the direction along which the deformation is purely stretching deformation. If the isotherms form an angle of less then 45° with the axis of dilatation, the deformation is frontogenetical. Otherwise it is frontolytical.

b. Frontal Circulations

The association of frontal zones with upward motions is to be expected from quasi-geostrophic theory. According to Sutcliffe's (1947) development equation, vertical velocity is generated by vorticity advection by the thermal wind. Sawyer (1956) showed that this effect is important near fronts in his quasi-geostrophic analysis of frontal circulations.

Eliassen (1959) expanded Sawyer's work by assuming geostrophic balance across the front but not along it. Williams (1967) showed that the quasi-geostrophic equations cannot describe a frontal collapse in a finite time. It is believed (Heckley and Hoskins, 1982) that Eliassen's inclusion of ageostrophic advection of the geostrophic wind captures the essential nonlinearities of the problem. Eliassen developed a two-dimensional, elliptic equation, now known as the Sawyer-Eliassen equation, for streamlines of the transverse frontal circulation. The forcing of the equation is given by a single term Q, which can be expressed in terms of the geostrophic wind and temperature distributions. If Q is positive the circulation is thermally direct. Negative Q forces a thermally indirect circulation. Shapiro (1982) related the forcing term to the deformation and showed that stretching deformation leads to

$Q>0$ and a direct circulation, while shearing deformation leads to $Q<0$.

The intimate relation between frontogenesis and symmetric instability is illustrated by the fact that the ellipticity condition on the Sawyer-Eliassen equation is symmetric stability. Thus symmetric instability changes the fundamental character of the equation governing frontal circulations but violates some assumptions behind the derivation of the equations.

The Sawyer-Eliassen equation has been expanded to three dimensions by Heckley and Hoskins (1982), among others. Hoskins et. al. (1978) described the relationship between vertical velocity and ageostrophy. Ageostrophy can occur when the shear generated to satisfy thermal wind balance exceeds that which is needed to balance the pressure gradient. Vertical motions reflect the atmosphere's attempt to restore geostrophic balance. Hoskins et. al. (1978) derived an equation for w in terms of the forcing function $\underset{\sim}{Q}$.

$$N^2\nabla_2 w + f^2\frac{\partial^2 w}{\partial z^2} = 2\nabla\cdot\underset{\sim}{Q} \tag{35}$$

where

$$\underset{\sim}{Q} = (Q_1, Q_2) = -\frac{g}{\theta_0}\left(\frac{\partial \underset{\sim}{v}_g}{\partial x}\cdot\nabla\theta, \frac{\partial \underset{\sim}{v}_g}{\partial y}\cdot\nabla\theta\right) \tag{36}$$

∇_2 is the horizontal divergence (in phyicial coordinates) and $N^2 = g/\theta_0(d\theta/dz)$ is the Brunt-Vaisala frequency squared. Upward motions are favored where $\underset{\sim}{Q}$ is convergent.

c. Frontal Structure

On the surface maps (Figs 3a-b), warm fronts are located south of Massachusetts and across Georgia and Alabama. On the vertical cross sections (Figs. 10a-b), the frontal layers slope towards the north and become more diffuse with height.

At 00 GMT, CHH is in the cold air, just north of the surface front. CHH's 00 GMT sounding of temperature, humidity and velocity is shown in Fig. 14a. The front appears on the sounding as a 7°C inversion and a 45° wind shift at 800 mb. Note that the atmosphere above the inversion is only slightly stable. On the PWM sounding (not shown), the frontal layer is manifested as a 7°C inversion in the layer between 825 mb and 740 mb.

At 12 GMT, the front is much weaker. The 12 GMT sounding for CHH (Fig. 14b) shows only a 2°C inversion at 850 mb. There is no wind shift. The atmosphere is stable

Fig. 14 Soundings for CHH on 11 December 1982. Diagrams are as in Fig. 3c.

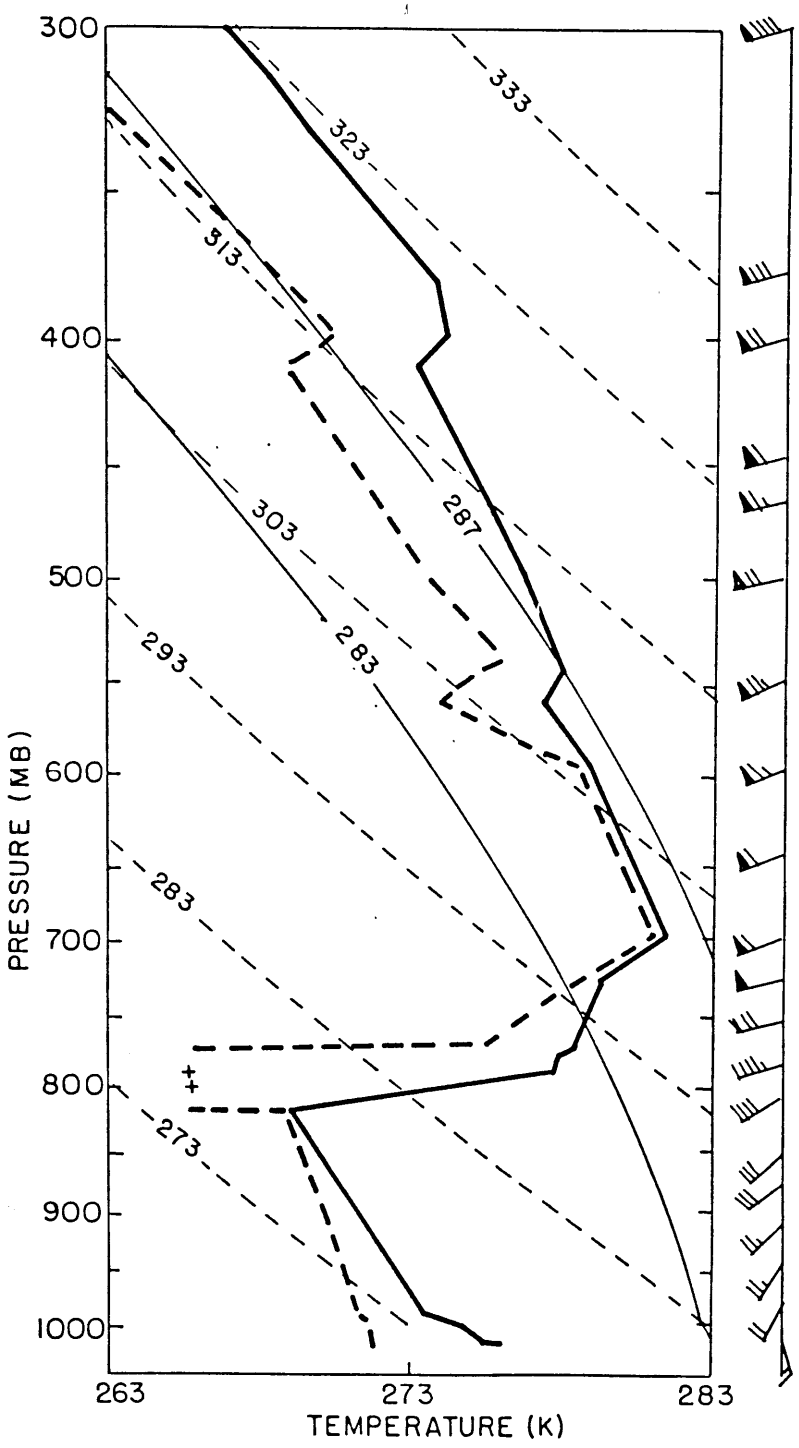

Fig. 14a 00 GMT

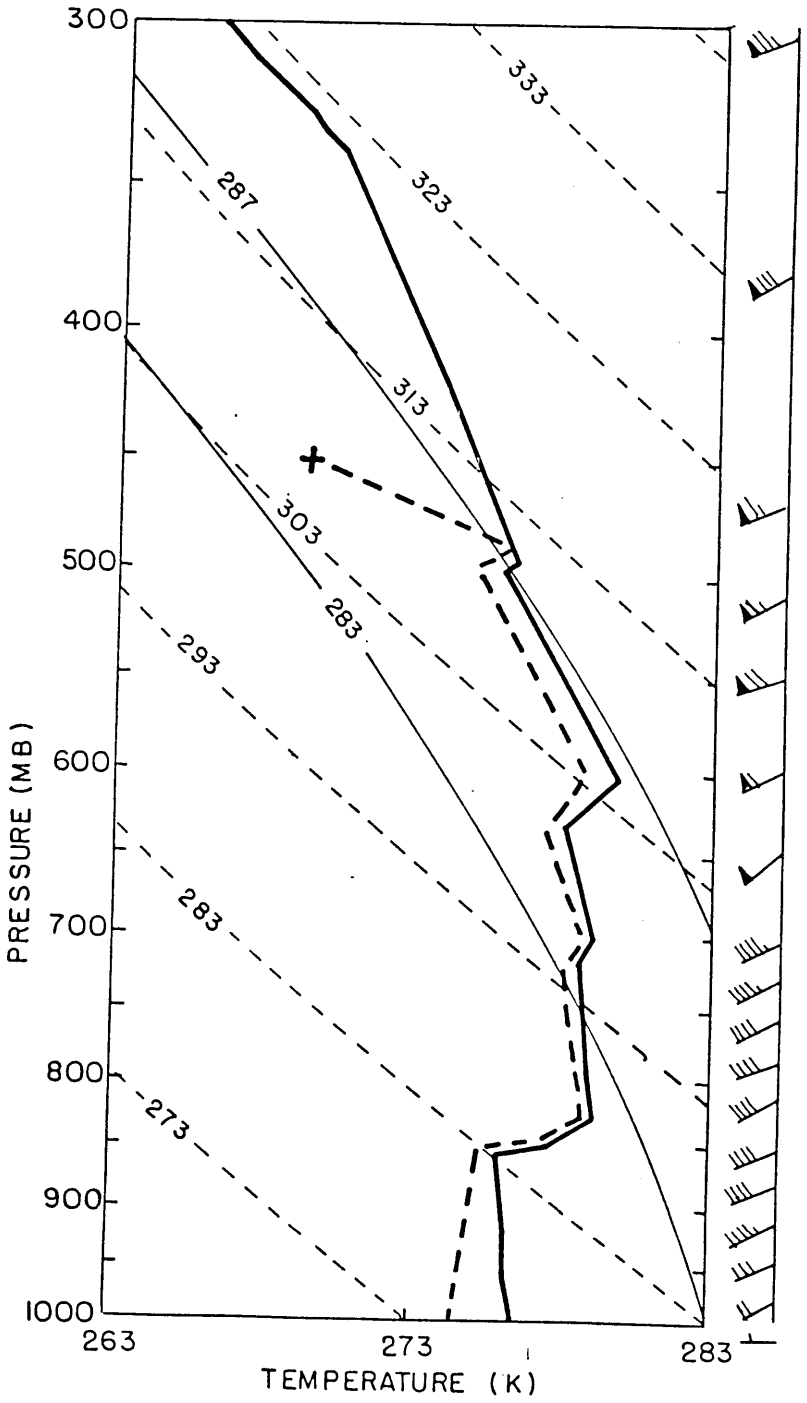

Fig. 14b 12 GMT

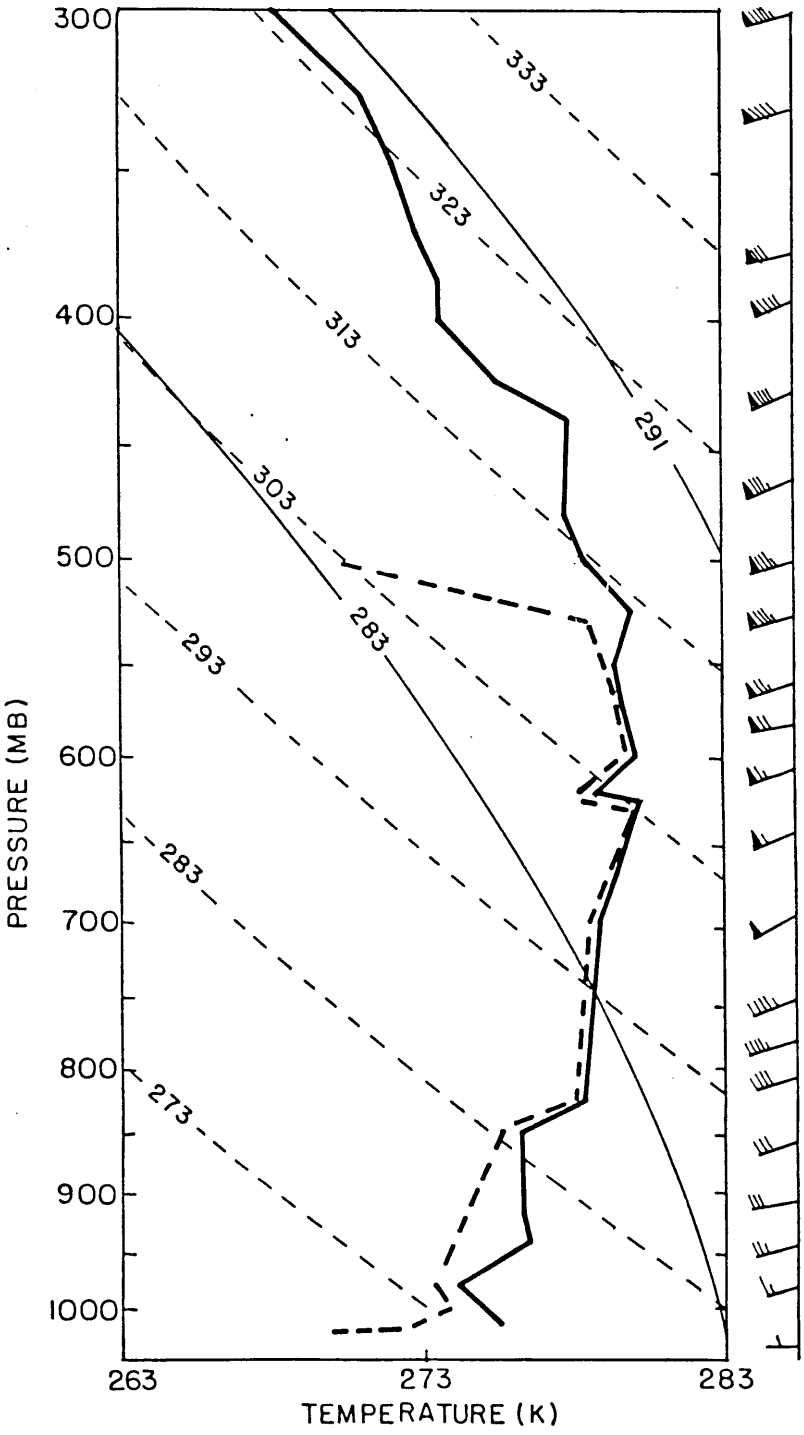

Fig. 14c 18 GMT

below 650 mb. The 12 GMT soundings for MIT and PWM (not shown) had 1°C and 2°C inversions, respectively, at 800 mb. Neither had a wind shift. Both were stable below 400 mb and almost moist adiabatic above 400 mb.

CHH's 18 GMT sounding (Fig. 14c) shows little frontal structure. The atmosphere is stable below 525 mb and almost neutral above 500 mb.

In the period between 00 GMT and 18 GMT, the front decays and the thermal stability of the lower to middle troposphere, the region of the band circulations, increases.

d. Frontogenetical Forcing of Upward Motion

Fields of deformation, horizontal divergence, and Q are calculated subjectively according to the formulae above. Geostrophic winds are determined from the geopotential analyses. The velocity components and potential temperature are contoured subjectively. The derivatives are approximated by centered finite differences, calculated graphically. Each field is shifted 2° latitude and subtracted from itself. Addition and subtraction are performed graphically. Multiplication, division, and trigonometry are accomplished with point-by-point calculations at station locations. The resultant fields are then contoured.

Fig. 15 Frontogenetical forcing at 00 GMT. Geostrophic deformation (solid lines) in units of 4.5×10^{-6} s^{-1} and potential isotherms (dashed lines) in K. Dilatation axes are shown with arrows.

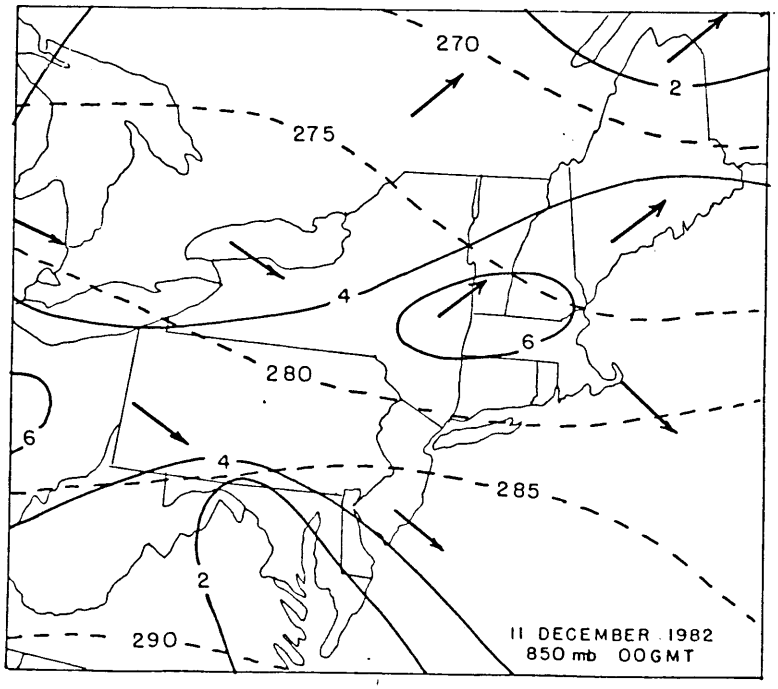

Fig. 15a

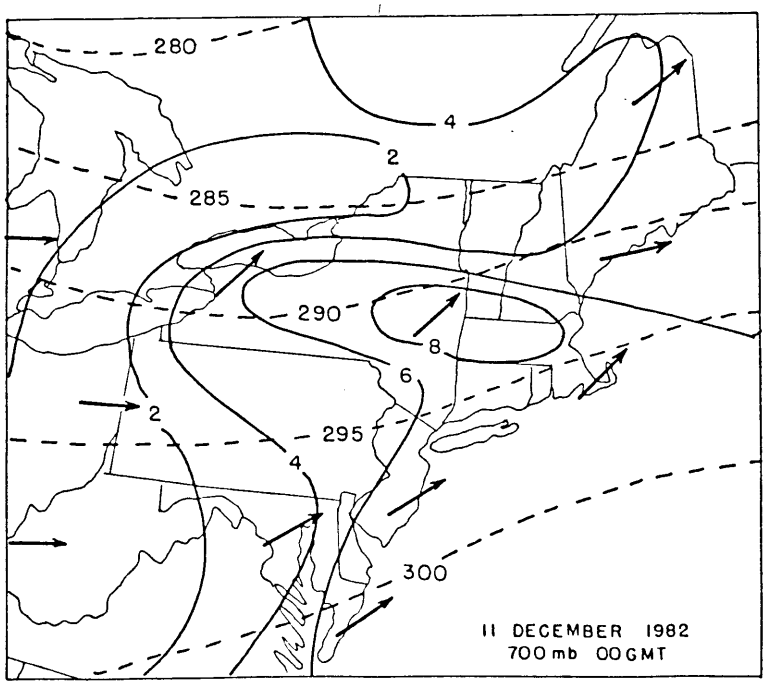

Fig. 15b
Potential temperature, geostrophic deformation, and dilatation axes

Figs. 15a-b show potential isotherms, geostrophic deformation magnitude, and dilatation axes for 00 GMT at 850 mb and 700 mb. At 850 mb, there is a swath of high deformation across central New England, Pennsylvania, and Ohio. The deformation is frontogenetical at PWM and MIT but frontolytical at CHH and ALB. The region of high deformation at 700 mb covers mainly central New England and the Eastern Seaboard. The deformation is frontogenetical throughout this region. The maximum geostrophic deformation at both levels is about 4×10^{-5} s^{-1}.

There is almost no deformation at 500 mb. The actual deformation at 00 GMT (not shown) is similar to the geostrophic deformation. At 12 GMT there is very little geostrophic deformation at 850 mb, 700 mb or 500 mb. The geostrophic deformation at that time is well to the west, and associated with the advancing cold front. The magnitude of the actual deformation (not shown) over New England is also about 4×10^{-5} s^{-1}. This deformation is due to ageostrophic convergence, which is discussed below.

e. Strength of the Frontogenetical Circulations

Figs. 16a-d show $\nabla \cdot \underset{\sim}{Q}$ for 00 GMT and 12 GMT at 850 mb and 700 mb. There is geostrophic frontogenetical forcing of upward motion where $\underset{\sim}{Q}$ is convergent. The regions of

Fig. 16 $\nabla \cdot \underset{\sim}{Q}$ in units of 3×10^{-16} $s^{-3}m^{-1}$

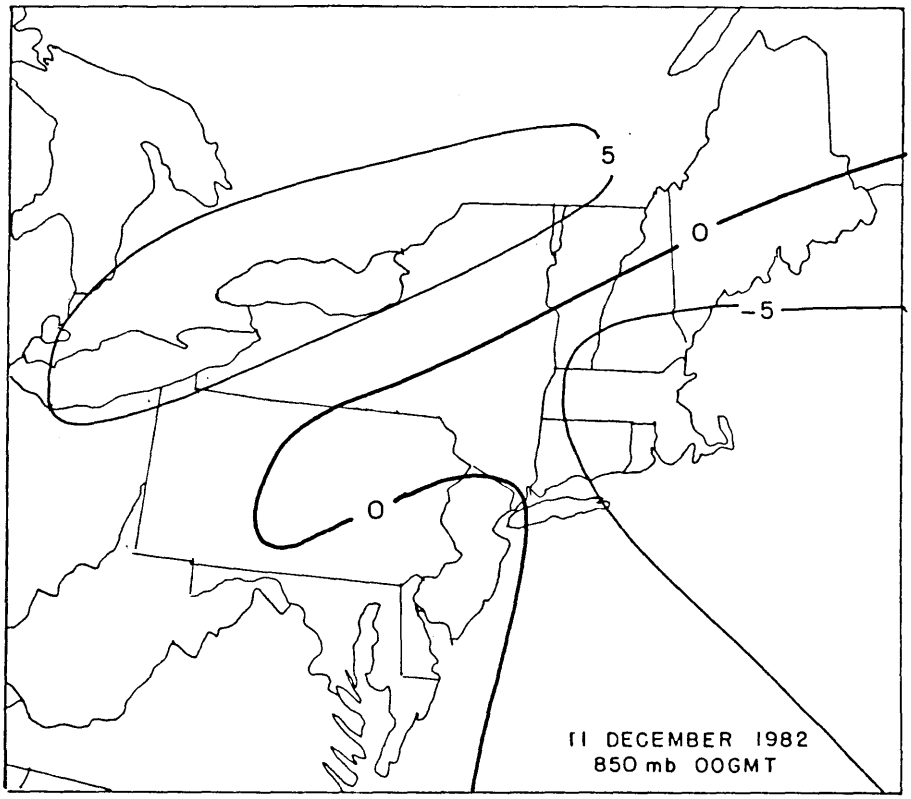

Fig. 16a

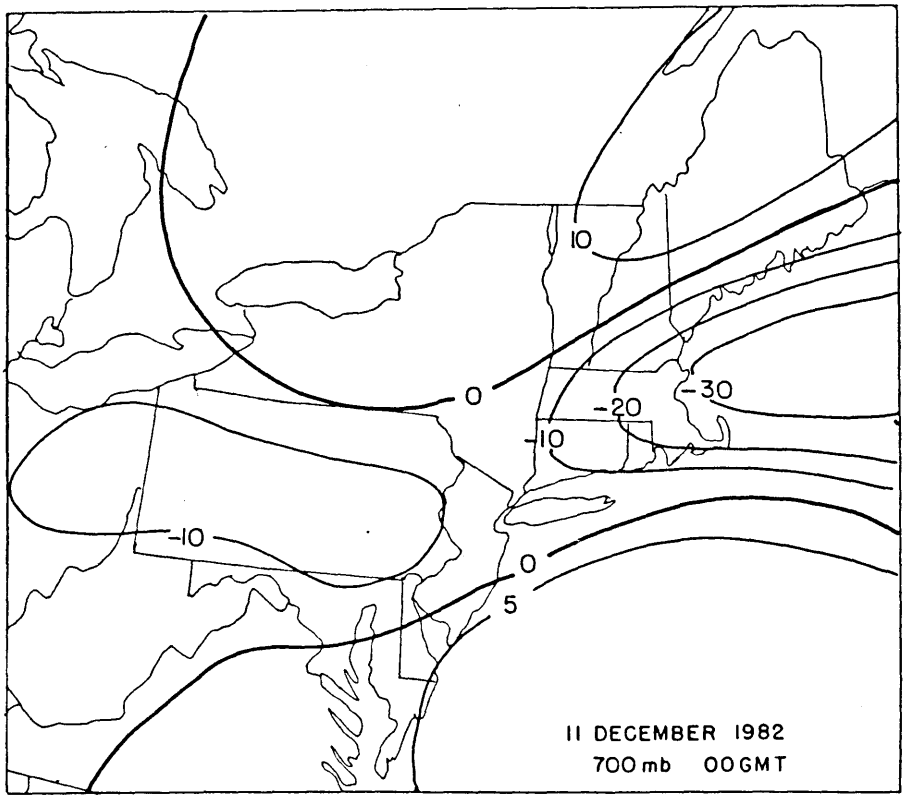

Fig. 16b

$\sigma \cdot \tilde{Q}$

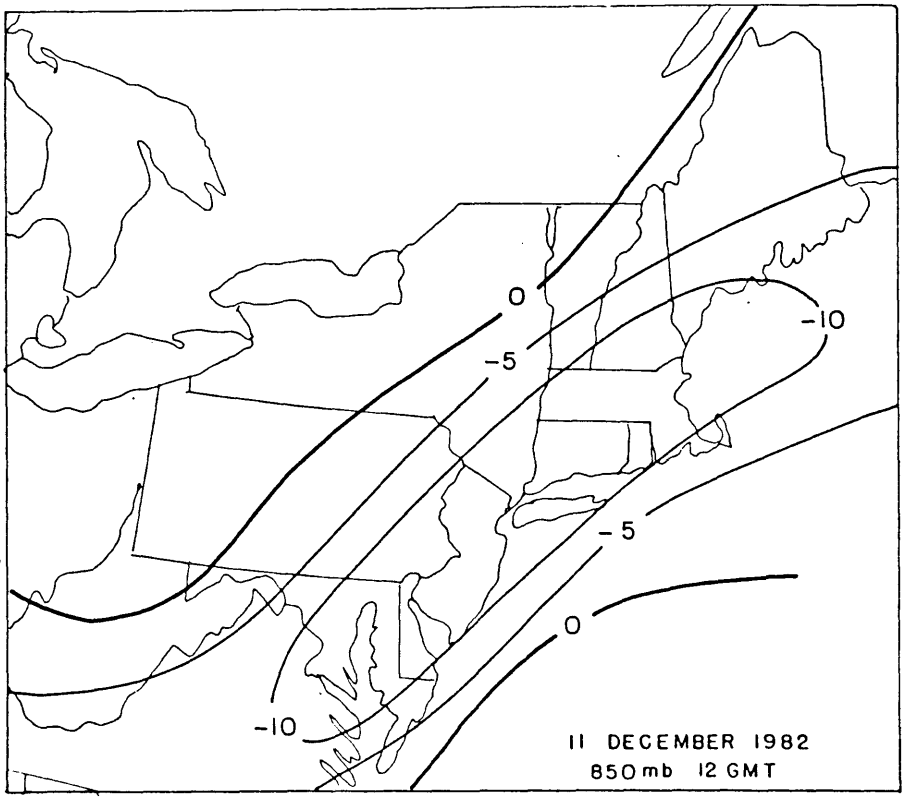

Fig. 16c

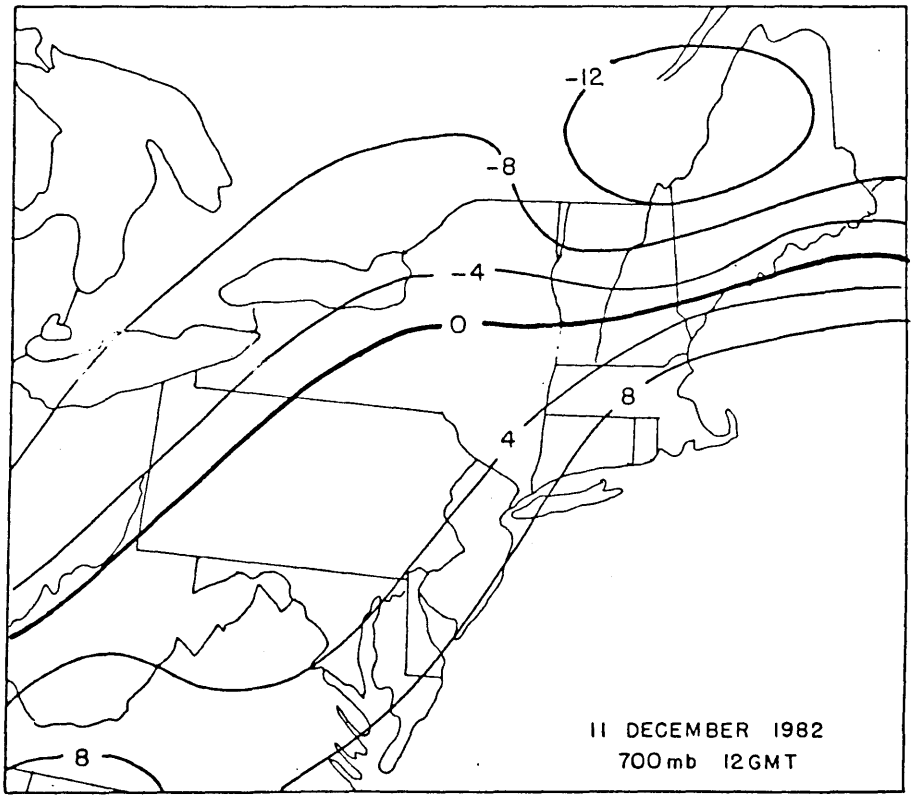

Fig. 16d

convergent $\underset{\sim}{Q}$ correspond roughly to the maxima in geostrophic deformation. However, the $\underset{\sim}{Q}$ convergence is not constrained to areas where the deformation is frontogenetical. At 12 GMT the region of convergent $\underset{\sim}{Q}$ is further north than at 00 GMT.

The strength of the vertical velocity resulting from $\nabla\cdot\underset{\sim}{Q}$ can be estimated by assuming both terms on the left-hand side of Eq. (33) are of the same magnitude. Then

$$f^2\frac{\partial^2 w}{\partial z^2} \approx 2\nabla\cdot\underset{\sim}{Q} \text{ or } W \approx \frac{H^2}{f^2}(\nabla\cdot\underset{\sim}{Q}) \tag{37}$$

If $H \approx 2$ km and $\nabla\cdot Q \approx 10^{-15}\ m^{-1}s^{-3}$ as suggested by Fig. 13

$$W \approx \frac{(2\times10^3 m)^2}{(10^{-4}s^{-1})^2}\ 10^{-15}m^{-1}s^{-3} \approx .4ms^{-1} \tag{38}$$

Figures 17a-d show divergence for 00 GMT and 12 GMT at 850 mb and 700 mb. Note that the convergence occurs in regions where there is frontogenetical forcing. There is convergence in New England, in the neighborhood of the warm front, and in Pennsylvania and Ohio, ahead of the cold front. The maximum convergence is at 850 mb. The convergence fields at 00 GMT and 12 GMT are similar.

Fig 17 $\nabla \cdot \underset{\sim}{v}$ in units of 4.5×10^{-6} s^{-1}

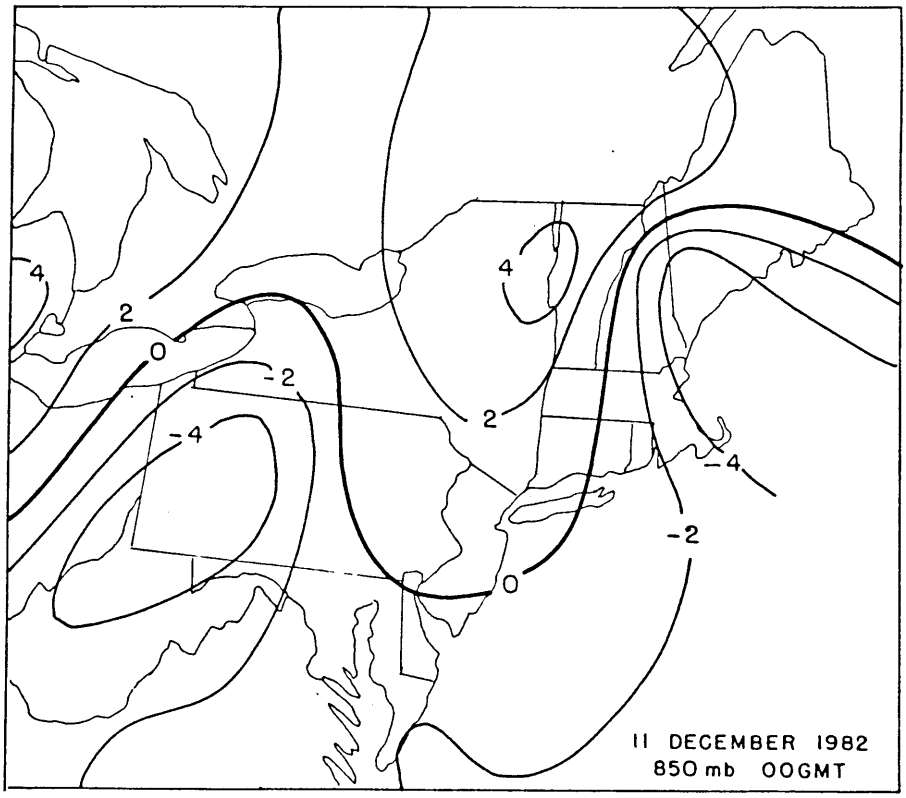

Fig. 17a

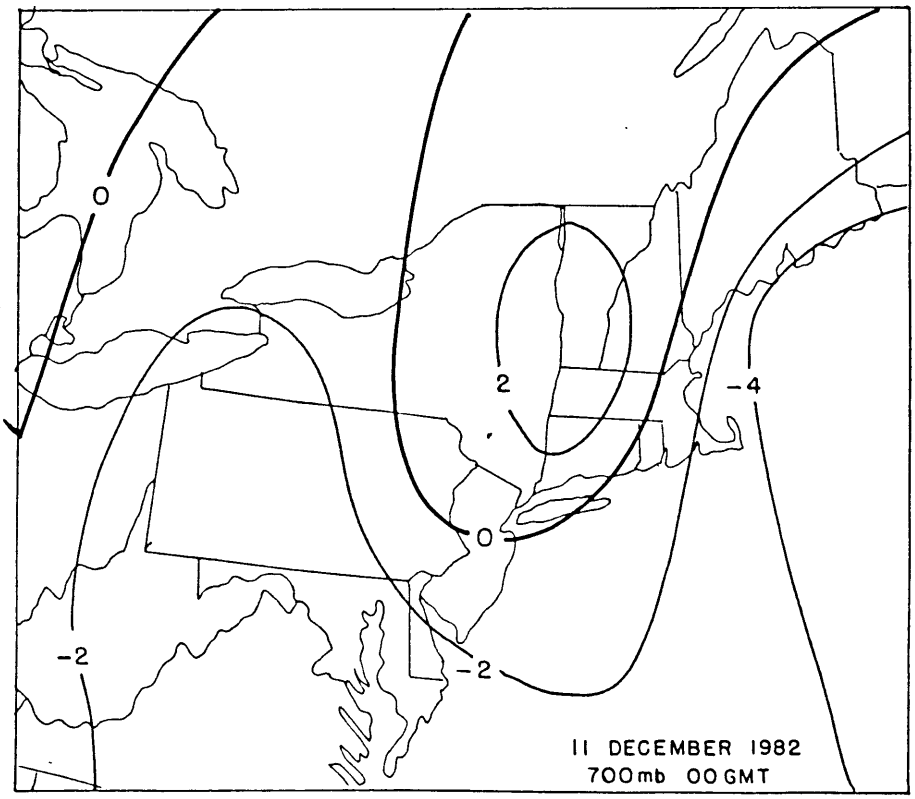

Fig. 17b

Divergence

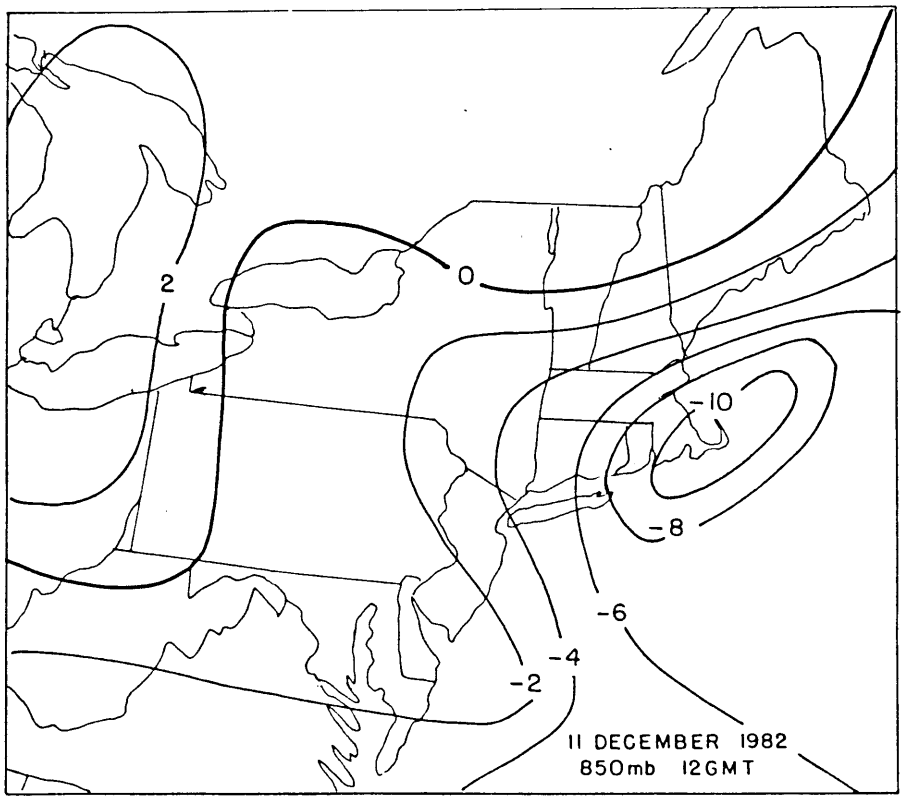

Fig. 17c

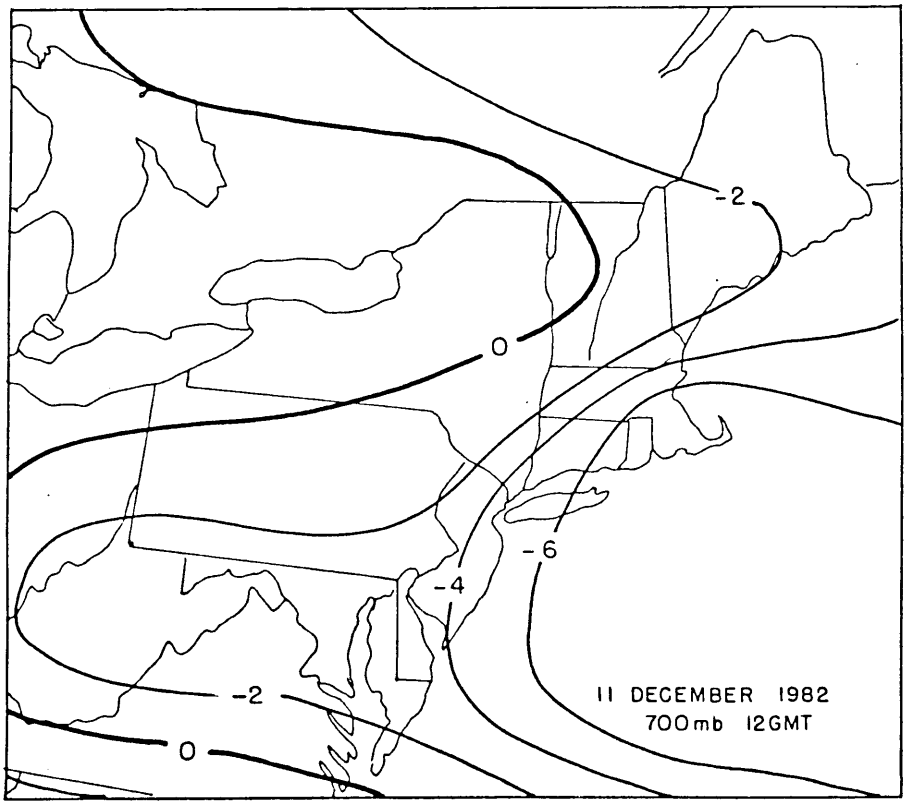

Fig. 17d

Divergence

The strength of the vertical velocity in New England can also be estimated from the divergence. At 850mb,

$$W \approx \left(\frac{\partial w}{\partial z}\right)_{850}\Delta z \approx 4.5\text{x}10^{-4}\text{s}^{-1}\cdot 1500\text{m} \approx .07\text{ms}^{-1} \qquad (39)$$

and at 700 mb,

$$W \approx \left(\frac{\partial w}{\partial z}\right)_{700}\Delta z + w_{850} \approx 2\text{x}10^{-5}\cdot 1500\text{m} + .07\text{ms}^{-1} \approx .1\text{ms}^{-1} \qquad (40)$$

These values agree well with the .05 ms^{-1} vertical velocity between bands calculated in the VVP analysis. (Fig. 5b)

f. Effect of the Frontogenetically Forced Circulation

In previous papers on moist symmetric instability (Emanuel, 1983b,d; Bennetts and Hoskins, 1979) it is postulated that the environment is brought to saturation and that unstable parcels are lifted to the level of free convection by synoptic scale ascent. The sub-synoptic scale documented here plays that roll in this case. In the soundings along surfaces of $M_g = -10ms^{-1}$, (Figs. 11a-b) the most unstable parcels are at about 650 mb 00 GMT and 850 mb at 12 GMT. Neither of these parcels is saturated. To release the instability, they must be lifted dry-adiabatically along the M_g surface to their condensation

levels. In both cases, a parcel lifted along an M_g surface sees an almost dry-adiabatic atmospheric lapse rate, so this displacement is opposed by very little negative buoyancy. The frontogenetical circulation has both a vertical component and an ageostrophic component in the x-direction so it could lift the parcels as required.

In the previous section it was demonstrated that a negative correlation of w and $\partial\theta_e/\partial Z$ decreases SPA. The magnitude of this effect is estimated here. The terms in which w enters the time rate of change of SPA in eq. (24) are $w(g/\theta_0)(\Gamma_m/\Gamma_d)(\partial\theta_{e0}/\partial Z)$ and $w(L_v/C_p)(\partial q_s/\partial Z)$. For typical atmospheric values, these terms are of the same order of magnitude. In the unstable regions, $\Gamma_m/\Gamma_d \approx .8$ and $\partial\theta_e/\partial Z \approx -.25 Kkm^{-1}$. The vertical velocity estimated above is $W \approx .1 ms^{-1}$. The change in SPA due to the frontogentically forced upward motion is estimated from eq. (24) as

$$\frac{d_p}{dt} SPA \approx W\frac{g}{\theta_v}\frac{\partial\theta}{\partial Z} \approx .1ms^{-1}\frac{9.8ms^{-1}}{288K}(-.25x10^{-3}Km^{-1})(2x10^{3}m) \quad (41)$$

$$\approx -1.7 \times 10^{-3}\ m^2s^{-3}$$

The decrease in SPA due to vertical velocity is an order of magnitude smaller than the generation of SPA due to geostrophic lapse rate advection given in eq. (29).

The frontogenesis may enhance the geostrophic lapse rate advection. Note in Fig. 2a that the isotherms at 850 mb are

oriented approximately west to east over New England. At 00 GMT, frontogenesis is increasing the temperature gradient. The thermal wind relation requires an increase in the component of the geostrophic wind along the isotherms to balance the temperature gradient. Frontogenesis affects primarily the lower portion of the troposphere. By increasing the westerly component of the winds at lower levels with respect to the winds at upper levels, frontogenesis increases the degree to which the geostrophic wind backs with height.

VI. DISCUSSION AND CONCLUSIONS

Symmetric instability explains many features observed in the bands of this case. Substantial portions of the atmosphere were conditionally unstable according to the criteria of the parcel model of symmetric instability in two-dimensional flow. The bands formed in the unstable layers. As indicated by aircraft and radar data, bands took the form of sloped rolls almost parallel to the mean shear, as predicted by the theory.

A few observations remain unexplained. Length and time scales were smaller than those expected for symmetric instability. As discussed in chapter IV, the slope of the displacement is expected to be intermediate between the slopes of the M_g and θ_e surfaces. However the streamlines found in the airplane band passes were steeper than the either the M_g or θ_e surfaces. The current model does not explain the different numbers of bands observed at various times. Time-dependent behavior in the roll structures was sometimes observed on movies made from series of CAPPI displays. The stability of two dimensional rolls to smaller perturbations is not known.

The rate at which potential energy was generated and converted to kinetic energy was estimated. There appears to have been a rough equilibrium between its generation and

depletion. However the conditions for symmetric instability were derived under the assumption of two-dimensional flow. The condition responsible for potential energy generation, counter-clockwise rotation of the shear vector, violates this assumption.

A region of sub-synoptic scale ascent, attributed to frontogenetical forcing was deduced. This intermediate scale process could have contributed to formation of bands by lifting conditionally unstable parcels to a level where potential energy could be released. Frontogenesis may also have enhanced the geostrophic lapse rate advection which generated the potential energy. The relation between frontogenetical forcing and band formation is highlighted by the fact that the bands became smaller and weaker as the warm front diffused during the later periods of the case study. The progressive decrease in band width and strength did not seem to be related to parameters relevant to symmetric instability such as vertical shear or stratification. The ageostrophy, apparently attributable to frontogenesis, also results in a base state which violates conditions under which symmetric instability has been derived.

The degree to which observed band characteristics correspond to predictions of symmetric instablity suggests that the results of the theory have some relevance even when there are deviations from the idealizations. Future

analytical work and computer simulations should address the hypothesis that three-dimensional and ageostrophic base states may be symmetrically unstable. The effect of the former condition is particularly relevant because it allows lapse rate advection and hence generation of the instability. In the absence of this mechanism, instability is created mainly by surface heating and friction. These processes are an unlikely source of any bands which form over land in the winter.

There has been speculation (Bosart, 1984) as to whether the presence of bands affects the amount of precipitation from a storm. It seems likely that in this case, there would have been no precipitation in New England had the band forming mechanisms discussed been inactive.

Acknowledgements

The author thanks her advisor, Dr. Kerry Emanuel, for his assistance and advice during the course of this research. Dr. Richard Passarelli directed the New England Winter Storm Experiment and was a source of ideas and encouragement. Dr. Frederick Sanders also made useful comments. Stephen Garner and Peter Neilley provided insightful discussion and were of invaluable assistance in taking the data. Isabelle Kole drafted the figures. This work was supported by NSF/g 8209375-ATM.

References

Austin, P. M., 1960: Microstructure as described by quantitative radar data. Geophys. Monogr., 5, 86-92.

Bennetts, D. A., and B. J. Hoskins, 1979: Conditional symmetric instability -- a possible explanation for frontal rainbands. Quart. J. Roy. Met. Soc., 105, 945-962.

Bosart, L. F., 1984: review of Session 2: Fronts and banded structures in cyclonic storms, part 2. (see Emanuel, First conference on mesoscale meteorology, 31 May - 3 June, 1983, Norman, Oklahoma), Bull. Am. Met. Soc., 65, p. 146

Carbone, R. E., 1982: A severe frontal rainband. Part I: storm wide hydrodynamic structure. J. Atmos. Sci., 39, 258-279.

Eliassen,A.,1959: On the vertical circulation in frontal zones. Geofys. Publikasjoner, 24, No. 4, 147-160.

Elliot, R. D. and E. L. Hovind, 1964: On convection within Pacific Coast storms and their relation to structure. J. App. Met., 3, 143-154.

Emanuel, K. A., 1979: Inertial instability and mesoscale convective systems. Part I: Linear theory of inertial instability in rotating viscous fluids. J. Atmos. Sci., 36, 2425-2449.

_____, 1983: On assessing local conditional symmetric instability from atmospheric soundings. Mon. Wea. Rev., 111, in press.

_____, 1983: The Lagrangian parcel dynamics of moist symmetric instability. J. Atmos. Sci., 40, 2368-2376.

_____, 1983: Symmetric instability. D.K. Lilly and T. Gal-Chen (eds.), Mesoscale Meteorology - Theories, Observations and Models, 217-229.

_____, 1983: Conditional symmetric Instability: A theory for rainbands within extratropical cyclones. D.K. Lilly and T. Gal-Chen (eds.) Mesoscale Meteorology - Theories, Observations and Models, 231-245.

Heckley, W. A. and B. J. Hoskins,1982: Baroclinic waves in a non-uniform potential vorticity semi-geostrophic model, J. Atmos. Sci., 39, 1999-2016.

Hoskins, B. J., 1975: The geostrophic momentum approximation and the semi-geostrophic equations, J. Atmos. Sci., 32, 233-242.

_____ , I. Draghici, and H. C. Davies, 1978: A new look at the ω equation. Quart. J. Roy. Met. Soc., 104, 31-38.

_____ and N. W. West, 1979: Baroclinic waves and frontogenesis. Part II: Uniform potential vorticity jet flows - cold and warm fronts. J. Atmos. Sci., 36, 1663-1680.

Houze, R. A., P. V. Hobbs, K. R. Biwas, W. M. Davis, 1976: Mesoscale rainbands in extratropical cyclones, Mon. Wea. Rev., 104, 868-878.

Lindzen, R. S., and K. K. Tung, 1976: Banded convective activity and ducted gravity waves. Mon. Wea. Rev., 104, 1602-1617.

Sawyer, J. S., 1956: The vertical circulation at meteorological fronts and its relation to frontogenesis., Proc. Roy. Soc. London, A234, 346-362.

Shapiro, M. A., 1981: Frontogenesis and geostrophically forced secondary circulations in the vicinity of jet stream frontal zone systems. J. Atmos. Sci., 38, 954-973.

Stone, P. H., 1966: Frontogenesis by horizontal wind deformation fields, J. Atmos. Sci., 23, 455-465.

Sutcliffe, R. C., 1947: A contribution to the problem of development, Quart. J. Roy. Met. Soc., 73, 370-383.

Waldtuefel, P. and H. Corbin, 1979: On the analysis of single- Doppler radar data. J. Appl. Met., 18, 532-542.

Williams, R. T., 1967: Atmospheric frontogenesis: A numerical experiment. J. Atmos. Sci., 24, 627-641.

Williams, R. T., 1968: A note on quasi-geostrophic frontogenesis, J. Atmos. Sci. 23, 455-465.